Title

Search for Continuous and Transient Neutrino Emission Associated with IceCube's Highest-energy Tracks: An 11 yr Analysis

Journal

The Astrophysical Journal, 964(1)

ISSN

0004-637X

Authors

Abbasi, R
Ackermann, M
Adams, J
et al.

Publication Date

2024-03-01

DOI

10.3847/1538-4357/ad18d6

Draft version February 6, 2024
Typeset using LaTeX default style in AASTeX631

arXiv:2309.12130v2 [astro-ph.HE] 5 Feb 2024

Search for Continuous and Transient Neutrino Emission Associated with IceCube's Highest-Energy Tracks: An 11-Year Analysis

R. Abbasi,[17] M. Ackermann,[63] J. Adams,[18] S. K. Agarwalla,[40,*] J. A. Aguilar,[12] M. Ahlers,[22] J.M. Alameddine,[23] N. M. Amin,[44] K. Andeen,[42] G. Anton,[26] C. Argüelles,[14] Y. Ashida,[53] S. Athanasiadou,[63] S. N. Axani,[44] X. Bai,[50] A. Balagopal V.,[40] M. Baricevic,[40] S. W. Barwick,[30] V. Basu,[40] R. Bay,[8] J. J. Beatty,[20,21] J. Becker Tjus,[11,†] J. Beise,[61] C. Bellenghi,[27] C. Benning,[1] S. BenZvi,[52] D. Berley,[19] E. Bernardini,[48] D. Z. Besson,[36] E. Blaufuss,[19] S. Blot,[63] F. Bontempo,[31] J. Y. Book,[14] C. Boscolo Meneguolo,[48] S. Böser,[41] O. Botner,[61] J. Böttcher,[1] E. Bourbeau,[22] J. Braun,[40] B. Brinson,[6] J. Brostean-Kaiser,[63] R. T. Burley,[2] R. S. Busse,[43] D. Butterfield,[40] M. A. Campana,[49] K. Carloni,[14] E. G. Carnie-Bronca,[2] S. Chattopadhyay,[40,*] N. Chau,[12] C. Chen,[6] Z. Chen,[55] D. Chirkin,[40] S. Choi,[56] B. A. Clark,[19] S. Coenders,[27] A. Coleman,[61] G. H. Collin,[15] A. Connolly,[20,21] J. M. Conrad,[15] P. Coppin,[13] P. Correa,[13] D. F. Cowen,[59,60] P. Dave,[6] C. De Clercq,[13] J. J. DeLaunay,[58] D. Delgado,[14] S. Deng,[1] K. Deoskar,[54] A. Desai,[40] P. Desiati,[40] K. D. de Vries,[13] G. de Wasseige,[37] T. DeYoung,[24] A. Diaz,[15] J. C. Díaz-Vélez,[40] M. Dittmer,[43] A. Domi,[26] H. Dujmovic,[40] M. A. DuVernois,[40] T. Ehrhardt,[41] A. Eimer,[26] P. Eller,[27] E. Ellinger,[62] S. El Mentawi,[1] D. Elsässer,[23] R. Engel,[31,32] H. Erpenbeck,[40] J. Evans,[19] P. A. Evenson,[44] K. L. Fan,[19] K. Fang,[40] K. Farrag,[16] A. R. Fazely,[7] A. Fedynitch,[57] N. Feigl,[10] S. Fiedlschuster,[26] C. Finley,[54] L. Fischer,[63] D. Fox,[59] A. Franckowiak,[11] A. Fritz,[41] P. Fürst,[1] J. Gallagher,[39] E. Ganster,[1] A. Garcia,[14] L. Gerhardt,[9] A. Ghadimi,[58] C. Glaser,[61] T. Glauch,[27] T. Glüsenkamp,[26,61] N. Goehlke,[32] J. G. Gonzalez,[44] S. Goswami,[58] D. Grant,[24] S. J. Gray,[19] O. Gries,[1] S. Griffin,[40] S. Griswold,[52] K. M. Groth,[22] C. Günther,[1] P. Gutjahr,[23] C. Haack,[26] A. Hallgren,[61] R. Halliday,[24] L. Halve,[1] F. Halzen,[40] H. Hamdaoui,[55] M. Ha Minh,[27] K. Hanson,[40] J. Hardin,[15] A. A. Harnisch,[24] P. Hatch,[33] A. Haungs,[31] K. Helbing,[62] J. Hellrung,[11] F. Henningsen,[27] L. Heuermann,[1] N. Heyer,[61] S. Hickford,[62] A. Hidvegi,[54] C. Hill,[16] G. C. Hill,[2] K. D. Hoffman,[19] S. Hori,[40] K. Hoshina,[40,‡] W. Hou,[31] T. Huber,[31] K. Hultqvist,[54] M. Hünnefeld,[23] R. Hussain,[40] K. Hymon,[23] S. In,[56] A. Ishihara,[16] M. Jacquart,[40] O. Janik,[1] M. Jansson,[54] G. S. Japaridze,[5] M. Jeong,[53] M. Jin,[14] B. J. P. Jones,[4] N. Kamp,[14] D. Kang,[31] W. Kang,[56] X. Kang,[49] A. Kappes,[43] D. Kappesser,[41] L. Kardum,[23] T. Karg,[63] M. Karl,[27] A. Karle,[40] A. Katil,[25] U. Katz,[26] M. Kauer,[40] J. L. Kelley,[40] A. Khatee Zathul,[40] A. Kheirandish,[34,35] J. Kiryluk,[55] S. R. Klein,[8,9] A. Kochocki,[24] R. Koirala,[44] H. Kolanoski,[10] T. Kontrimas,[27] L. Köpke,[41] C. Kopper,[26] D. J. Koskinen,[22] P. Koundal,[31] M. Kovacevich,[49] M. Kowalski,[10,63] T. Kozynets,[22] J. Krishnamoorthi,[40,*] K. Kruiswijk,[37] E. Krupczak,[24] A. Kumar,[63] E. Kun,[11] N. Kurahashi,[49] N. Lad,[63] C. Lagunas Gualda,[63] M. Lamoureux,[37] M. J. Larson,[19] S. Latseva,[1] F. Lauber,[62] J. P. Lazar,[14,40] J. W. Lee,[56] K. Leonard DeHolton,[60] A. Leszczyńska,[44] M. Lincetto,[11] Q. R. Liu,[40] M. Liubarska,[25] E. Lohfink,[41] C. Love,[49] C. J. Lozano Mariscal,[43] L. Lu,[40] F. Lucarelli,[28] W. Luszczak,[20,21] Y. Lyu,[8,9] J. Madsen,[40] K. B. M. Mahn,[24] Y. Makino,[40] E. Manao,[27] S. Mancina,[40,48] W. Marie Sainte,[40] I. C. Mariş,[12] S. Marka,[46] Z. Marka,[46] M. Marsee,[58] I. Martinez-Soler,[14] R. Maruyama,[45] F. Mayhew,[24] T. McElroy,[25] F. McNally,[38] J. V. Mead,[22] K. Meagher,[40] S. Mechbal,[63] A. Medina,[21] M. Meier,[16] Y. Merckx,[13] L. Merten,[11] J. Micallef,[24] J. Mitchell,[7] T. Montaruli,[28] R. W. Moore,[25] Y. Morii,[16] R. Morse,[40] M. Moulai,[40] T. Mukherjee,[31] R. Naab,[63] R. Nagai,[16] M. Nakos,[40] U. Naumann,[62] J. Necker,[63] A. Negi,[4] M. Neumann,[43] H. Niederhausen,[24] M. U. Nisa,[24] A. Noell,[1] A. Novikov,[44] S. C. Nowicki,[24] A. Obertacke Pollmann,[16] V. O'Dell,[40] M. Oehler,[31] B. Oeyen,[29] A. Olivas,[19] R. Orsoe,[27] J. Osborn,[40] E. O'Sullivan,[61] H. Pandya,[44] N. Park,[33] G. K. Parker,[4] E. N. Paudel,[44] L. Paul,[50] C. Pérez de los Heros,[61] J. Peterson,[40] S. Philippen,[1] A. Pizzuto,[40] M. Plum,[50] A. Pontén,[61] Y. Popovych,[41] M. Prado Rodriguez,[40] B. Pries,[24] R. Procter-Murphy,[19] G. T. Przybylski,[9] C. Raab,[37] J. Rack-Helleis,[41] K. Rawlins,[3] Z. Rechav,[40] A. Rehman,[44] P. Reichherzer,[11] G. Renzi,[12] E. Resconi,[27] S. Reusch,[63] W. Rhode,[23] B. Riedel,[40] A. Rifaie,[1] E. J. Roberts,[2] S. Robertson,[8,9] S. Rodan,[56] G. Roellinghoff,[56] M. Rongen,[26] C. Rott,[53,56] T. Ruhe,[23] L. Ruohan,[27]

analysis@icecube.wisc.edu

D. Ryckbosch,[29] I. Safa,[14,40] J. Saffer,[32] D. Salazar-Gallegos,[24] P. Sampathkumar,[31] S. E. Sanchez Herrera,[24] A. Sandrock,[62] M. Santander,[58] S. Sarkar,[25] S. Sarkar,[47] J. Savelberg,[1] P. Savina,[40] M. Schaufel,[1] H. Schieler,[31] S. Schindler,[26] L. Schlickmann,[1] B. Schlüter,[43] F. Schlüter,[12] N. Schmeisser,[62] T. Schmidt,[19] J. Schneider,[26] F. G. Schröder,[31,44] L. Schumacher,[26] G. Schwefer,[1] S. Sclafani,[19] D. Seckel,[44] M. Seikh,[36] S. Seunarine,[51] R. Shah,[49] S. Shefali,[32] N. Shimizu,[16] M. Silva,[40] B. Skrzypek,[14] B. Smithers,[4] R. Snihur,[40] J. Soedingrekso,[23] A. Søgaard,[22] D. Soldin,[32] P. Soldin,[1] G. Sommani,[11] C. Spannfellner,[27] G. M. Spiczak,[51] C. Spiering,[63] M. Stamatikos,[21] T. Stanev,[44] T. Stezelberger,[9] T. Stürwald,[62] T. Stuttard,[22] G. W. Sullivan,[19] I. Taboada,[6] S. Ter-Antonyan,[7] M. Thiesmeyer,[1] W. G. Thompson,[14] J. Thwaites,[40] S. Tilav,[44] K. Tollefson,[24] C. Tönnis,[56] S. Toscano,[12] D. Tosi,[40] A. Trettin,[63] C. F. Tung,[6] R. Turcotte,[31] J. P. Twagirayezu,[24] M. A. Unland Elorrieta,[43] A. K. Upadhyay,[40,*] K. Upshaw,[7] A. Vaidyanathan,[42] N. Valtonen-Mattila,[61] J. Vandenbroucke,[40] N. van Eijndhoven,[13] D. Vannerom,[15] J. van Santen,[63] J. Vara,[43] J. Veitch-Michaelis,[40] M. Venugopal,[31] M. Vereecken,[37] S. Verpoest,[44] D. Veske,[46] A. Vijai,[19] C. Walck,[54] C. Weaver,[24] P. Weigel,[15] A. Weindl,[31] J. Weldert,[60] A. Y. Wen,[14] C. Wendt,[40] J. Werthebach,[23] M. Weyrauch,[31] N. Whitehorn,[24] C. H. Wiebusch,[1] D. R. Williams,[58] L. Witthaus,[23] A. Wolf,[1] M. Wolf,[27] G. Wrede,[26] X. W. Xu,[7] J. P. Yanez,[25] E. Yildizci,[40] S. Yoshida,[16] R. Young,[36] S. Yu,[24] T. Yuan,[40] Z. Zhang,[55] P. Zhelnin[14] And P. Zilberman[40]
et al.
IceCube Collaboration

[1] III. Physikalisches Institut, RWTH Aachen University, D-52056 Aachen, Germany
[2] Department of Physics, University of Adelaide, Adelaide, 5005, Australia
[3] Dept. of Physics and Astronomy, University of Alaska Anchorage, 3211 Providence Dr., Anchorage, AK 99508, USA
[4] Dept. of Physics, University of Texas at Arlington, 502 Yates St., Science Hall Rm 108, Box 19059, Arlington, TX 76019, USA
[5] CTSPS, Clark-Atlanta University, Atlanta, GA 30314, USA
[6] School of Physics and Center for Relativistic Astrophysics, Georgia Institute of Technology, Atlanta, GA 30332, USA
[7] Dept. of Physics, Southern University, Baton Rouge, LA 70813, USA
[8] Dept. of Physics, University of California, Berkeley, CA 94720, USA
[9] Lawrence Berkeley National Laboratory, Berkeley, CA 94720, USA
[10] Institut für Physik, Humboldt-Universität zu Berlin, D-12489 Berlin, Germany
[11] Fakultät für Physik & Astronomie, Ruhr-Universität Bochum, D-44780 Bochum, Germany
[12] Université Libre de Bruxelles, Science Faculty CP230, B-1050 Brussels, Belgium
[13] Vrije Universiteit Brussel (VUB), Dienst ELEM, B-1050 Brussels, Belgium
[14] Department of Physics and Laboratory for Particle Physics and Cosmology, Harvard University, Cambridge, MA 02138, USA
[15] Dept. of Physics, Massachusetts Institute of Technology, Cambridge, MA 02139, USA
[16] Dept. of Physics and The International Center for Hadron Astrophysics, Chiba University, Chiba 263-8522, Japan
[17] Department of Physics, Loyola University Chicago, Chicago, IL 60660, USA
[18] Dept. of Physics and Astronomy, University of Canterbury, Private Bag 4800, Christchurch, New Zealand
[19] Dept. of Physics, University of Maryland, College Park, MD 20742, USA
[20] Dept. of Astronomy, Ohio State University, Columbus, OH 43210, USA
[21] Dept. of Physics and Center for Cosmology and Astro-Particle Physics, Ohio State University, Columbus, OH 43210, USA
[22] Niels Bohr Institute, University of Copenhagen, DK-2100 Copenhagen, Denmark
[23] Dept. of Physics, TU Dortmund University, D-44221 Dortmund, Germany
[24] Dept. of Physics and Astronomy, Michigan State University, East Lansing, MI 48824, USA
[25] Dept. of Physics, University of Alberta, Edmonton, Alberta, Canada T6G 2E1
[26] Erlangen Centre for Astroparticle Physics, Friedrich-Alexander-Universität Erlangen-Nürnberg, D-91058 Erlangen, Germany
[27] Physik-department, Technische Universität München, D-85748 Garching, Germany
[28] Département de physique nucléaire et corpusculaire, Université de Genève, CH-1211 Genève, Switzerland
[29] Dept. of Physics and Astronomy, University of Gent, B-9000 Gent, Belgium
[30] Dept. of Physics and Astronomy, University of California, Irvine, CA 92697, USA
[31] Karlsruhe Institute of Technology, Institute for Astroparticle Physics, D-76021 Karlsruhe, Germany
[32] Karlsruhe Institute of Technology, Institute of Experimental Particle Physics, D-76021 Karlsruhe, Germany
[33] Dept. of Physics, Engineering Physics, and Astronomy, Queen's University, Kingston, ON K7L 3N6, Canada
[34] Department of Physics & Astronomy, University of Nevada, Las Vegas, NV, 89154, USA
[35] Nevada Center for Astrophysics, University of Nevada, Las Vegas, NV 89154, USA

[36] *Dept. of Physics and Astronomy, University of Kansas, Lawrence, KS 66045, USA*
[37] *Centre for Cosmology, Particle Physics and Phenomenology - CP3, Université catholique de Louvain, Louvain-la-Neuve, Belgium*
[38] *Department of Physics, Mercer University, Macon, GA 31207-0001, USA*
[39] *Dept. of Astronomy, University of Wisconsin–Madison, Madison, WI 53706, USA*
[40] *Dept. of Physics and Wisconsin IceCube Particle Astrophysics Center, University of Wisconsin–Madison, Madison, WI 53706, USA*
[41] *Institute of Physics, University of Mainz, Staudinger Weg 7, D-55099 Mainz, Germany*
[42] *Department of Physics, Marquette University, Milwaukee, WI, 53201, USA*
[43] *Institut für Kernphysik, Westfälische Wilhelms-Universität Münster, D-48149 Münster, Germany*
[44] *Bartol Research Institute and Dept. of Physics and Astronomy, University of Delaware, Newark, DE 19716, USA*
[45] *Dept. of Physics, Yale University, New Haven, CT 06520, USA*
[46] *Columbia Astrophysics and Nevis Laboratories, Columbia University, New York, NY 10027, USA*
[47] *Dept. of Physics, University of Oxford, Parks Road, Oxford OX1 3PU, United Kingdom*
[48] *Dipartimento di Fisica e Astronomia Galileo Galilei, Università Degli Studi di Padova, 35122 Padova PD, Italy*
[49] *Dept. of Physics, Drexel University, 3141 Chestnut Street, Philadelphia, PA 19104, USA*
[50] *Physics Department, South Dakota School of Mines and Technology, Rapid City, SD 57701, USA*
[51] *Dept. of Physics, University of Wisconsin, River Falls, WI 54022, USA*
[52] *Dept. of Physics and Astronomy, University of Rochester, Rochester, NY 14627, USA*
[53] *Department of Physics and Astronomy, University of Utah, Salt Lake City, UT 84112, USA*
[54] *Oskar Klein Centre and Dept. of Physics, Stockholm University, SE-10691 Stockholm, Sweden*
[55] *Dept. of Physics and Astronomy, Stony Brook University, Stony Brook, NY 11794-3800, USA*
[56] *Dept. of Physics, Sungkyunkwan University, Suwon 16419, Korea*
[57] *Institute of Physics, Academia Sinica, Taipei, 11529, Taiwan*
[58] *Dept. of Physics and Astronomy, University of Alabama, Tuscaloosa, AL 35487, USA*
[59] *Dept. of Astronomy and Astrophysics, Pennsylvania State University, University Park, PA 16802, USA*
[60] *Dept. of Physics, Pennsylvania State University, University Park, PA 16802, USA*
[61] *Dept. of Physics and Astronomy, Uppsala University, Box 516, S-75120 Uppsala, Sweden*
[62] *Dept. of Physics, University of Wuppertal, D-42119 Wuppertal, Germany*
[63] *Deutsches Elektronen-Synchrotron DESY, Platanenallee 6, 15738 Zeuthen, Germany*

(Dated: February 6, 2024)

ABSTRACT

IceCube alert events are neutrinos with a moderate-to-high probability of having astrophysical origin. In this study, we analyze 11 years of IceCube data and investigate 122 alert events and a selection of high-energy tracks detected between 2009 and the end of 2021. This high-energy event selection (alert events + high-energy tracks) has an average probability of ≥ 0.5 to be of astrophysical origin. We search for additional continuous and transient neutrino emission within the high-energy events' error regions. We find no evidence for significant continuous neutrino emission from any of the alert event directions. The only locally significant neutrino emission is the transient emission associated with the blazar TXS 0506+056, with a local significance of 3σ, which confirms previous IceCube studies. When correcting for 122 test positions, the global p-value is 0.156 and is compatible with the background hypothesis. We constrain the total continuous flux emitted from all 122 test positions at 100 TeV to be below 1.2×10^{-15} (TeV cm^2 s)$^{-1}$ at 90% confidence assuming an E^{-2} spectrum. This corresponds to 4.5% of IceCube's astrophysical diffuse flux. Overall, we find no indication that alert events, in general, are linked to lower-energetic continuous or transient neutrino emission.

Keywords: Neutrino Astronomy (1100) — High-energy astrophysics (739) — Transient sources (1851) — Blazars (164) — Active galactic nuclei (16)

1. INTRODUCTION

The IceCube Neutrino Observatory (Aartsen et al. 2017a) is a Cherenkov detector using a cubic kilometer of Antarctic ice at the geographic South Pole to primarily (but not exclusively) study high-energy astrophysical neutrinos. Its duty cycle is greater than 99% (Aartsen et al. 2017a), and its field of view covers the full sky while being most sensitive to high-energy neutrino events near the celestial equator. This makes IceCube ideal for surveying the sky (Aartsen et al. 2017b). As part of the realtime program, IceCube alerts other telescopes upon detection of a neutrino event with a high probability of being of astrophysical origin, which can then trigger follow-up observations (Aartsen et al. 2017b; Blaufuss et al. 2019; Kintscher 2016).

On the 22nd of September 2017, IceCube detected a neutrino of likely astrophysical origin (IceCube-170922A[1]). This triggered multi-wavelength follow-up observations, which detected a flaring blazar (TXS 0506+056) at the reconstructed origin direction of IceCube-170922A (Aartsen et al. 2018a). This correlation is significant at a 3σ level (Aartsen et al. 2018a). Additionally, a neutrino flare was identified originating from the same direction between September 2014 and March 2015 with a significance of 3.5σ (Aartsen et al. 2018b).

This detection demonstrates that IceCube alerts can point to neutrino source candidates due to their high probability of being of astrophysical origin, and we aim to investigate the origin directions of other IceCube alerts. A preliminary search showed no indication of continuous neutrino emission (Karl 2019). However, the IceCube alert criteria have since been updated (Blaufuss et al. 2019; Abbasi et al. 2023a). The IceCube data have also been reprocessed with improved calibration of the optical sensors (Abbasi et al. 2021a; Aartsen et al. 2020). This leads to improved energy and direction reconstruction compared to previous results in Aartsen et al. (2018b); Abbasi et al. (2021b); Aartsen et al. (2020, 2015); Abbasi et al. (2021d,c). A first analysis benefiting from this new processing (Abbasi et al. 2022a) detected the neutrino signal from the Seyfert II galaxy NGC 1068 with a significance of 4.2σ (compared to 2.9σ in Aartsen et al. (2020)). A large part of the increase (0.9σ) is due to improved data processing and calibration. More details about effects on data are discussed in appendix B and in the supplementary material of Abbasi et al. (2022a).

In this work, we analyze 11 years of reprocessed IceCube data (through-going muon tracks, see Table 1) and search for an excess of neutrino-induced muons. We apply a conservative lower limit on the angular uncertainty of 0.2 degrees, whereas the median angular resolution is 0.57 degrees (compared to a median angular resolution of 0.59 degrees before the reprocessing). We identify possible neutrino production sites by looking at the origin of high-energy neutrinos that have a high probability of being of astrophysical origin. IceCube's highest energy neutrinos with the largest astrophysical purity are events from the new selection of IceCube alerts published in the so-called "gold" alert channel (Blaufuss et al. 2019; Abbasi et al. 2023a). Additionally, we extend the list by including 18 high-energy events from Abbasi et al. (2022b) that were confirmed to be likely astrophysical events by a new event classifier (Kronmueller & Glauch 2019). Since we use a combination of IceCube alert events and high-energy tracks identified retrospectively, we will refer to our event selection as "alert+ events" for brevity. All IceCube data used in this work (lower and high-energy events) have been reprocessed.

In this work, we excluded alert+ events within 30 degrees of the geographic poles (affecting three events), for which we have smaller statistics for the background. Other IceCube analyses have applied different declination cuts (for example including all events up to 81° declination (Abbasi et al. 2022a) or up to 82° (Aartsen et al. 2020)). Additionally, we removed alert+ events with large uncertainties (≥ 100 square degrees, affecting two events). As a result, our final sample consists of 122 high-energy events (104 IceCube alert events and 18 high-energy tracks, listed in Table 3), detected between 2009 and the end of 2021. On average, our selected alert+ events have a probability to be astrophysical of $\gtrsim 0.5$. The probability to be astrophysical is spectrum dependent and based on the muon neutrino spectrum measured by IceCube (Haack & Wiebusch 2017; Abbasi et al. 2022b). The median angular resolution (90%

* also at Institute of Physics, Sachivalaya Marg, Sainik School Post, Bhubaneswar 751005, India
† also at Department of Space, Earth and Environment, Chalmers University of Technology, 412 96 Gothenburg, Sweden
‡ also at Earthquake Research Institute, University of Tokyo, Bunkyo, Tokyo 113-0032, Japan

[1] https://gcn.gsfc.nasa.gov/notices_amon/50579430_130033.amon

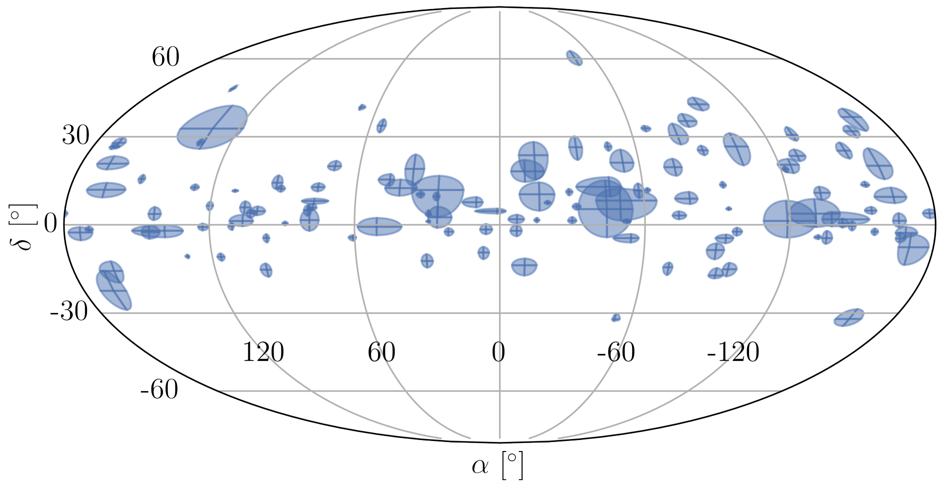

Figure 1. Sky map in right ascension and declination (epoch=J2000) with the arrival directions of events fulfilling the IceCube alert criteria (with the highest probability to be of astrophysical origin) we investigate in this work. The events were detected between August 2009 and the end of 2021. The shaded regions represent the 90% uncertainty region of the reconstruction.

uncertainty regions) of alert+ events is 2.1 degrees. In Figure 1, we show a map of all arrival directions and their 90% uncertainty regions of IceCube alert+ events investigated in this work. These events provide positions of interest analogous to a catalog of possible neutrino sources. Since IceCube alert+ events trigger this analysis, we remove the respective alert+ event from the 11 years of IceCube data when running the analysis. We present the analysis method in Section 2 and the results in Section 3.

Table 1. Overview of the improved and reprocessed data samples in this analysis. The columns list the configuration of the detector ("IC" and the number of deployed strings), the uptime (livetime) of the detector in days, the number of events in each sample, and the start and end dates of the data subset.

Year	Livetime [days]	Number of events	Start	End
IC59	353.578	107011	2009 May 5	2010 May 31
IC79	316.045	93133	2010 June 1	2011 May 13
IC86 2011-2019	3184.163	1133364	2011 May 13	2020 May 29

2. ANALYSIS METHOD

We use an unbinned likelihood approach as presented by Braun et al. (2008). In this work, we investigate two source types: continuous sources and transient sources. We compare two hypotheses (each with a set of parameters $\vec{\theta}$)

- **Background hypothesis** $H_0(\vec{\theta}_0)$: The background comprises atmospheric neutrinos, atmospheric muons (remaining after event selection cuts), and diffuse astrophysical neutrinos. The flux is uniform in time and right ascension.

- **Signal hypothesis** $H_1(\vec{\theta}_1)$: There is a signal component additional to the atmospheric background and the average diffuse astrophysical neutrino emission. The signal neutrinos cluster around their source (subscript S) at right ascension, declination $\vec{x}_S = (\alpha_S, \delta_S)$. The energy spectrum of the emitted flux is an unbroken power law: $\frac{d\phi}{dE_\nu} \propto E_\nu^{-\gamma}$. In the specific case of a transient source hypothesis (see Section 2.2), the neutrino emission has a Gaussian time profile with mean μ_T and width σ_T.

We remove the high-energy alert+ events that triggered this analysis from the data set. Hence, we look for additional neutrino emission from the direction of the high-energy alert+ events. We then maximize the likelihood, $\mathcal{L}$, and compute the likelihood ratio

$$\lambda(\vec{x}) = \frac{\sup \mathcal{L}(H_0)}{\sup \mathcal{L}(H_1)}. \tag{1}$$

The likelihood maximization varies the expectation value of the number of detected signal neutrinos, n_S, and the emitted energy spectral index, γ. We allow values for γ between 1.5 and 4. For the background hypothesis, n_S is fixed to 0.

The likelihood is the probability density of observing the data given a specific hypothesis. The probability density of observing an event, i, is a sum of its probability to be signal, S_i, or background, B_i: $\frac{n_S}{N} S_i + \left(1 - \frac{n_S}{N}\right) B_i$, where N is the total number of detected events (signal and background combined).

We define the test statistic, TS, as

$$\mathrm{TS} = -2 \ln \lambda = -2 \ln \left[\frac{\mathcal{L}\left(\hat{\vec{\theta}}_0 | \vec{x}_S\right)}{\mathcal{L}\left(\hat{\vec{\theta}}_1 | \vec{x}_S\right)} \right] = 2 \ln \left[\frac{\mathcal{L}\left(n_S = \hat{n}_S\right)}{\mathcal{L}\left(n_S = 0\right)} \right] = 2 \sum_i \ln \left[\frac{\hat{n}_S}{N} \left(\frac{S_i}{B_i} - 1 \right) + 1 \right], \tag{2}$$

for a signal hypothesis with the best-fit value of $\hat{n}_S$ neutrinos (the "ˆ" denoting the best-fit of a parameter) as the mean number of neutrinos we expect to detect from the neutrino source.

The investigated source candidates have directional uncertainties (see Figure 1). However, we assume potential sources are smaller than the best resolution of 0.2 degrees in our data (TXS 0506+056 has an angular size of ~ 2.6 arc-seconds). Hence, we fit the best point-source position within a reconstructed 90% uncertainty region by dividing the region in a grid with steps of 0.2° in right ascension and declination, the best angular uncertainty for events used in this study. The likelihood is optimized at each grid point. The grid point yielding the best result (i.e., the highest TS value) is subsequently considered the point-source position.

This procedure is run on different realizations of background data $\sim 10^4$ times. The background data are all 11 years of muon tracks with randomly assigned right ascensions. In the final step, we calculate the test statistic value, $\mathrm{TS}_{\mathrm{data}}$, for the true data and compare this with the simulated background test statistic distribution. The local p-value is the probability of getting this $\mathrm{TS}_{\mathrm{data}}$ (or a larger value) from a random background realization. This procedure is repeated for all remaining regions in the sky, yielding 122 local p-values. From these 122 values, we take the most significant local p-value, p_0, to identify the most significant source.

As a next step, we correct the significance for having tested 122 regions in the sky. Considering only background realizations, we take the most significant p-value out of 122 positions for each realization and generate a distribution of best local p-values, $p_{0,\mathrm{BG}}$. The final global p-value of our analysis is the probability for $p_{0,\mathrm{BG}}$ to be at least as significant as the p-value we got from our real data, p_0. Since we are investigating only a limited number of points (122), weaker neutrino emissions have a higher significance in this analysis than in an all-sky scan, for example, in Abbasi et al. (2022a).

When testing the method with Monte Carlo simulations, the best-fit number of signal neutrinos, $\hat{n}_S$, and source spectral index, $\hat{\gamma}$, show a bias compared to the true simulated source properties. For sources with simulated hard spectral indices (i.e., $\gamma = 2$), there is a tendency to fit slightly softer spectra and a slightly larger number of signal neutrinos. For simulated sources following softer spectral indices (i.e., $\gamma = 3$), the tendency is reversed to fitting slightly harder spectral indices and smaller numbers of signal neutrinos. Appendix A presents a more in-depth discussion of this bias. Correcting the bias is not straightforward, and we have decided not to include an, at best, incomplete correction. Hence, the best-fit fluxes are only indicative. This bias does not affect the flux limits since they are based on simulated fluxes where the true source strength is known.

2.1. *Time-integrated search for continuous sources*

We define the signal and background probability density functions (pdfs) S_i and B_i in a spatial and an energy part (see, e.g., Braun et al. (2008); Abbasi et al. (2011)). The spatial part depends on the source position $\vec{x}_S$ and the reconstructed event properties: reconstructed origin $\vec{x}_i$ and the angular uncertainty of the reconstructed origin σ_i. The energy part depends on the reconstructed muon energy, E_i, the reconstructed origin declination, δ_i, and the source energy spectral index, γ. The signal pdf for a steady source is hence

$$S_i(\vec{x}_i, E_i | \sigma_i, \vec{x}_S, \gamma) = S_{\mathrm{spatial}}(\vec{x}_i | \sigma_i, \vec{x}_S) \cdot S_{\mathrm{energy}}(E_i | \delta_i, \gamma) = \frac{1}{2\pi\sigma_i^2} \exp\left(\frac{-|\vec{x}_i - \vec{x}_S|^2}{2\sigma_i^2} \right) \cdot S_{\mathrm{energy}}(E_i | \delta_i, \gamma). \tag{3}$$

The energy pdf, S_{energy}, is the probability of detecting a neutrino with reconstructed energy, E_i, at declination, δ_i, assuming the source emits neutrinos with a spectrum of $E^{-\gamma}$. The background pdfs, B_i, are defined similarly

$$B_i\left(\vec{x}_i, E_i\right) = B_{\text{spatial}}(\vec{x}_i) \cdot B_{\text{energy}}(E_i|\delta_i) = \frac{1}{2\pi} \cdot P(\delta_i) \cdot B_{\text{energy}}(E_i|\delta_i). \tag{4}$$

The spatial term depends only on the event declination, δ_i. We assume uniformity in right ascension for the background data due to IceCube's unique position at the South Pole. B_{energy} is derived directly from experimental data.

Searching for neutrino counterparts of the alert+ events, we want to be sensitive to a single strong emission from one (or a few) sources and, additionally, to faint emissions from a larger number of sources. Hence, our search for continuous sources consists of two parts. The first part searches for single strong neutrino emitters. The second part investigates the overall neutrino emission from all 122 positions of interest. In the latter case, we combine the neutrino emission and define a new test statistic value, $\text{TS}_{\text{stacked}}$, by summing the test statistic values of all alert+ positions, k,

$$\text{TS}_{\text{stacked}} = \sum_k \text{TS}_k. \tag{5}$$

We take the TS_k from the individual search, hence we do not correct for overlapping uncertainty regions of alert+ events.

2.2. *Transient sources*

For transient sources, we multiply a temporal pdf with the previously defined spatial and energy pdfs in equations (3) and (4) (Braun et al. 2010). We assume a Gaussian-shaped time profile centered around μ_T with width σ_T for the signal part. The temporal signal pdf becomes

$$S_T(t_i|\mu_T, \sigma_T) = \frac{1}{\sigma_T\sqrt{2\pi}} \exp\left(-\frac{\left(t_i - \mu_T\right)^2}{2\sigma_T^2}\right), \tag{6}$$

with t_i as the time the event was detected. The background expectation is a constant rate over the whole data taking time, t_{data}:

$$B_T = \frac{1}{\text{t}_{\text{data}}}. \tag{7}$$

The search for time-dependent sources adds another optimization step for the best flaring time. This introduces a bias towards shorter flares since the number of possible shorter flares is larger than the number of possible longer flares. We correct for this effect by multiplying the test statistic by a marginalization factor, $\frac{\sqrt{2\pi}\sigma_T}{300\text{ days}}$ (Braun et al. 2010). Here, 300 days is the maximal flaring time. Longer time scales would result in worse sensitivity than the time-integrated search. We assume a minimal σ_T of 5 days to ensure the background uniformity in right ascension.

Conventional methods to find neutrino flares as in Aartsen et al. (2015); Abbasi et al. (2021d); Aartsen et al. (2018b); Abbasi et al. (2021c) apply a brute-force scan of all possible time-intervals between events where the ratio of Equation (3) over Equation (4) exceeds a certain threshold. This is computationally expensive. The computational cost can be reduced by increasing the required threshold and hence reducing the possible number of intervals scanned. We want to include as few biases as possible, and if following conventional approaches, we would apply the same threshold as in Aartsen et al. (2018b), where the ratio had to be ≥ 1. However, Aartsen et al. (2018b) performs this search only on one position in the sky. In our case, this would mean scanning the uncertainty region of 122 alert+ events in steps of 0.2 degrees and, at each step, evaluating every possible time window between 5 and 300 days in 11 years for neutrino emission. This proved to be computationally unfeasible. To overcome this problem, we investigated new approaches (Karl et al. 2021; Karl 2022; Karl et al. 2023), which do not rely on thresholds, such as a different test statistic to evaluate if an emission is time-dependent (Eller & Shtembari 2021) or finding an analytical description of the test statistic such that we would not need to simulate a large number of background and signal models.

Here, we have applied an unsupervised learning algorithm looking for clustering in data: expectation maximization (Dempster et al. 1977). This is the first time we apply expectation maximization on IceCube data and use it to fit the best time of transient neutrino emission.

The procedure is as follows (Karl & Eller 2023). For a source position to be tested (grid point), we assume a two-component mixture model for the temporal distribution of our data (a neutrino flare in the form of a Gaussian signal and uniform background). As a starting flare, we choose a single very broad flare, extending beyond the whole data-taking period. For each event, we compute the probability of it belonging to the neutrino flare (the membership probability). These probabilities are then used to improve the flare parameters iteratively. In the calculation of the membership probability for event i, we include the pdf values for the spatial and energy signal and background pdfs (as in Equation (3) and Equation (4)) as event weights. The membership probability is:

$$P_{i,\mathrm{flare}} = \frac{\frac{n_{\mathrm{flare}}}{N} S_i S_T(t_i|\mu_T, \sigma_T)}{\frac{n_{\mathrm{flare}}}{N} S_i S_T(t_i|\mu_T, \sigma_T) + (1 - \frac{n_{\mathrm{flare}}}{N}) B_i B_T} = \frac{n_{\mathrm{flare}} \frac{S_i}{B_i} S_T(t_i|\mu_T, \sigma_T)}{n_{\mathrm{flare}} \frac{S_i}{B_i} S_T(t_i|\mu_T, \sigma_T) + \frac{N - n_{\mathrm{flare}}}{t_{\mathrm{data}}}}, \tag{8}$$

and at each iteration the mean time, μ_T, and the width, σ_T, are recalculated using

$$\mu_T = \frac{\sum_i P_{i,\mathrm{flare}} t_i}{\sum_i P_{i,\mathrm{flare}}}, \tag{9}$$

and

$$\sigma_T = \frac{\sum_i P_{i,\mathrm{flare}} \left(t_i - \mu_T\right)^2}{\sum_i P_{i,\mathrm{flare}}}. \tag{10}$$

The quantity n_{flare} scales the Gaussian temporal pdf according to the expected number of signal events. However, n_{flare} is only used to determine μ_T and σ_T; n_S is fitted independently once we determine the time pdf of the neutrino flare. We stop the iterations when there is no change in the likelihood in the past 20 iterations or once 500 iterations have been performed.

The signal weight, S_i/B_i, depends on the assumed source spectral index, γ. We want to avoid favoring a specific index; hence we run expectation maximization for different fixed spectral indices, γ_{EM}, between 1.5 and 4 in steps of 0.2 (Karl & Eller 2023). We get an optimized time pdf for each γ_{EM}. We then optimize the test statistic as in Equation (2) with the signal and background pdfs, including the temporal pdfs for each γ_{EM}. In this step, we fit n_S and γ while keeping the temporal pdf with $\hat{\mu}_T(\gamma_{\mathrm{EM}})$ and $\hat{\sigma}_T(\gamma_{\mathrm{EM}})$ fixed. The flare yielding the highest TS value is then the best-fit flare for this grid point. For each alert+, we repeat this procedure at every grid point in the uncertainty region. The point with the most significant result is then the preferred source location. For the background TS distribution, we shuffled the event times and calculated the new right ascension values based on the event azimuths and the shuffled times.

3. RESULTS

3.1. *Continuous sources*

The search for the strongest single continuous source yields a global p-value of 0.98 and is compatible with the background hypothesis. We determine an upper flux limit by simulating neutrino emission with an E^{-2} spectrum. The upper flux limit is the flux for which 90% of the corresponding test statistic distribution lies above the test statistic value of the strongest single continuous source. We get an upper flux limit (for muon neutrinos and antineutrinos) at 90% confidence level for the most significant position of $\Phi^{\nu_\mu+\bar{\nu}_\mu,\mathrm{single}}_{90\%,100\mathrm{TeV}} = 6.9 \times 10^{-17}$ (TeV cm^2 s)$^{-1}$. In general, the energy-dependent flux, $\Phi(E)$, of this flux limit is $\Phi(E) = \Phi^{\nu_\mu+\bar{\nu}_\mu,\mathrm{single}}_{90\%,100\mathrm{TeV}} \times \left(\frac{E}{100\ \mathrm{TeV}}\right)^{-2}$. The acceptance for the simulated flux has a limited range in energy. We define the energy range for the flux limit as the central 90% quantile of detected simulated events. In this case, we limit the flux from 0.9 TeV to 483 TeV. Table 4 lists the results for all 122 investigated regions.

For the combined emission of all sources, we get a p-value of 8%, which is also compatible with the background hypothesis. We determine the 90% confidence level upper flux limit, $\Phi^{\nu_\mu+\bar{\nu}_\mu,\mathrm{stacked}}_{90\%,100\mathrm{TeV}}$, by simulating an increasing number of sources emitting a weak flux, ϕ_1, corresponding to one neutrino coming from a source at the celestial equator — IceCube's most sensitive region for detecting neutrinos at the highest energies — in 11 years ($\phi_1 = 4.502 \times 10^{-18}$ (TeV cm^2 s)$^{-1}$). We repeat the simulation $\sim 10^4$ times for each combined flux and create a $\mathrm{TS}_{\mathrm{stacked}}$ distribution. Based on this distribution, we determine the combined flux strong enough to yield a higher test statistic value than our result with 90% probability.

The upper limit of emission additional to the alert+ events is $\Phi^{\nu_\mu+\bar{\nu}_\mu,\mathrm{stacked}}_{90\%,100\mathrm{TeV}} = 4.2 \times 10^{-16}$ (TeV cm^2 s)$^{-1}$ for a spectral index of $\gamma = 2$ and within the energy range from 4.2 TeV to 3.6 PeV. For comparison, the diffuse astrophysical neutrino flux is $\Phi_{\mathrm{diffuse,100TeV}} = 1.44 \times 10^{-15}$ (TeV cm^2 s sr)$^{-1}$ in the range of 15 TeV to 5 PeV (Abbasi et al. 2022b) with a

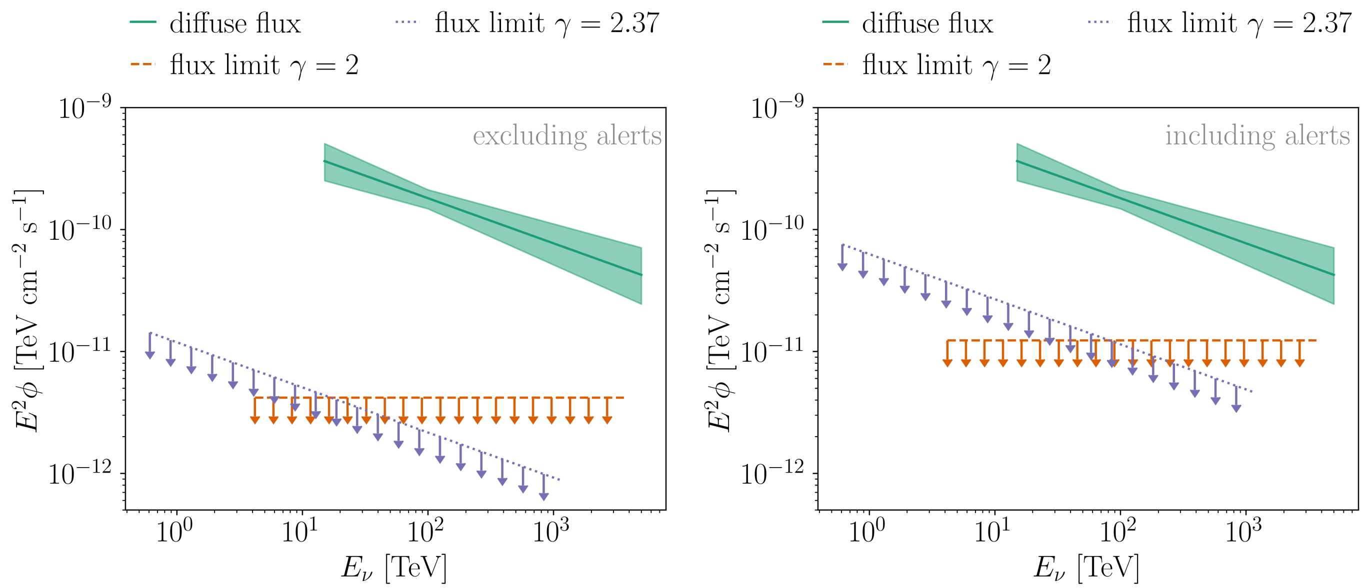

Figure 2. 90% confidence level upper flux limits assuming for all source candidates combined (dashed orange line) valid in the energy range of 4.2 TeV to 3.6 PeV and a neutrino emission following E^{-2}. The green line is the diffuse astrophysical neutrino flux ($\Phi_{\text{diffuse,100TeV}} = 1.44 \times 10^{-15} \cdot 4\pi$ (TeV cm^2 s)$^{-1}$) in the range of 15 TeV to 5 PeV (Abbasi et al. 2022b)). The dotted purple line shows the 90% confidence level upper flux limit for the spectral index of the diffuse flux ($\gamma = 2.37$) between 0.6 TeV and 1 PeV. **Left:** The upper flux limit, excluding the alert+ events in the analyzed data, is 1.6% ($\gamma = 2$) of the astrophysical diffuse flux in the overlapping energy range, and 1.5% when assuming the same spectral index ($\gamma = 2.37$) as for the astrophysical diffuse flux. **Right:** The upper flux limit, including the alert+ events in the data, is 4.5% of the astrophysical diffuse flux in the overlapping energy range for $\gamma = 2$, and 8% of the diffuse flux when assuming the same spectral index ($\gamma = 2.37$) as for the astrophysical diffuse flux.

spectral index of $\gamma = 2.37$. Integrating over the energy range where both the diffuse flux and $\Phi^{\nu_\mu+\bar{\nu}_\mu,\text{stacked}}_{90\%,100\text{TeV}}$ overlap, $\Phi^{\nu_\mu+\bar{\nu}_\mu,\text{stacked}}_{90\%,100\text{TeV}}$ corresponds to 1.6% of the astrophysical diffuse flux. To constrain the maximal possible emission from the alert+ regions, including the highest-energy events, we include the alert+ events just for the following limit. Thus, considering the total emission of all 122 regions, including alert+ events, we get an upper flux limit of $\Phi^{\nu_\mu+\bar{\nu}_\mu,\text{with alerts}}_{90\%,100\text{TeV}} = 1.2 \times 10^{-15}$ (TeV cm^2 s)$^{-1}$ for the energy range from 4.2 TeV to 3.6 PeV, which corresponds to 4.5% of the diffuse astrophysical neutrino flux where both fluxes overlap in their energy range (see Figure 2). We repeat the upper flux limit calculation with the same spectral index as for the astrophysical diffuse flux and get a limit of 2.1×10^{-16} (TeV cm^2 s)$^{-1}$ (1.5% of the astrophysical diffuse flux) excluding alert+ events, and 1.1×10^{-15} (TeV cm^2 s)$^{-1}$ including alert+ events (8% of the astrophysical diffuse flux) at 100 TeV. For $\gamma = 2.37$, the energies of the simulated detected events range from 0.6 TeV to 1 PeV. This energy range differs from the previous range for $\gamma = 2$. The energy distribution of the signal events depends on the simulated energy spectral index. There are more neutrinos in lower energies if the simulated energy spectrum is softer compared to a harder emission.

The lack of lower energy neutrino emission (compared to IceCube alert+ events) could be caused by various scenarios. It is, for example, possible that some sources flare in neutrinos, emitting mainly high-energy neutrinos. Another possibility might be a hard neutrino emission, i.e., $\gamma \leq 1$ (for example, models proposed in Waxman & Bahcall (1999); Padovani et al. (2022)). The atmospheric background would dominate the lower-energy neutrino emission. The higher-energy neutrino emission would be detected as single high-energy events, given IceCube's effective area (Aartsen et al. 2020; Abbasi et al. 2021b). This matches our observation. However, there are many different scenarios that agree with this work. In these cases, different source populations or states produce different neutrino spectra compared to one continuous power law. Another possible scenario including a source population emitting single power-laws is described in Abbasi et al. (2023b). Our result agrees with the high-density scenario presented in Section 6. There, a high-density source population with low individual fluxes (with an $E^{-2.5}$ energy spectrum) is the origin of alert events. Due to the sheer number of sources, we would be able to detect flux fluctuations in high-energies as alert events without a detectable lower-energy component. In lower energies, the flux would be too low to be detected and it would require

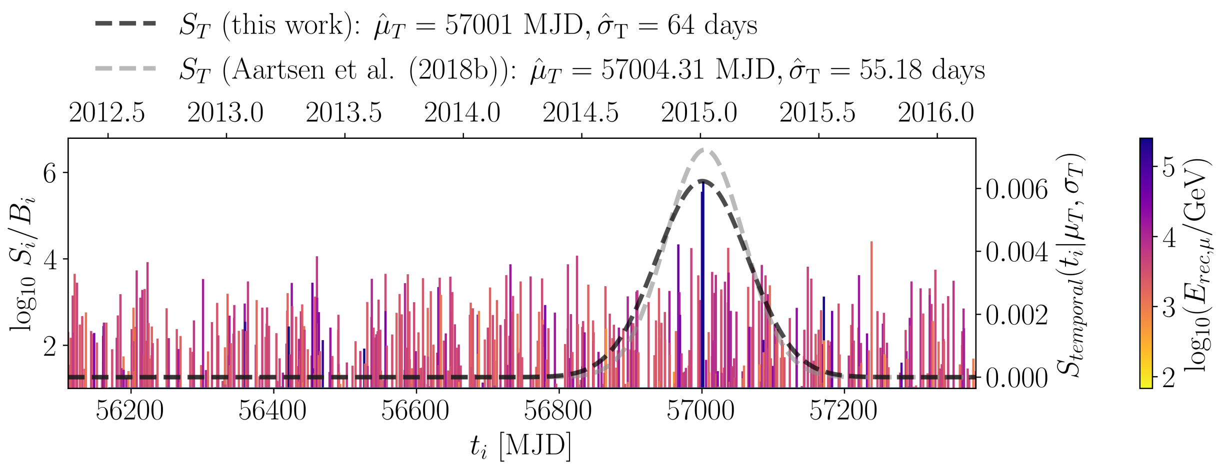

Figure 3. Logarithm of the signal-over-background ratio, $\log_{10} S_i/B_i$, distribution of individual events, i, versus their detection time, t_i, between 2012 and 2016. The $\log_{10} S_i/B_i$ values are for the best-fit position (close to TXS 0506+056) and the best-fit spectral index. The color indicates the reconstructed muon energy, $E_{\mathrm{rec},\mu}$, increasing from light to dark. The black-dashed line shows this work's best-fit time pdf S_T (with the y-axis on the right). It agrees with the grey-dashed pdf of Aartsen et al. (2018b).

a simultaneous fluctuation in both lower and higher energies such that both components could be detected from the same object.

3.2. *Transient sources*

In our search for transient sources, we look for the most significant transient neutrino emission. Out of all the investigated 122 alert+ origins, the most significant transient emission is the neutrino flare with the seed alert IceCube-170922A, which is associated with the blazar TXS 0506+056. Our search yields a local p-value of 0.14% (or a significance of 3σ). The main differences between the search in Aartsen et al. (2018b) and this work are:

- We have no external trigger in this work, whereas Aartsen et al. (2018b) was triggered by the observation of a flaring blazar.
- We use 11 years of recalibrated IceCube muon data, improving directional and energy reconstruction. For a discussion of how the contributing events are affected, see Appendix B.
- We include a fit for the best source position and use expectation maximization to identify the time of the neutrino flare.

The corresponding flare is centered around a mean flare time $\hat{\mu}_T = 57001^{+38}_{-26}$ MJD and has a width of $\hat{\sigma}_T = 64^{+35}_{-10}$ days. These properties agree with Aartsen et al. (2018b), as shown in Figure 3. When correcting for the look-elsewhere effect, the global p-value is $p_{\mathrm{global}} = 0.156$, which is not significant. Such a trial correction does not apply for the search reported in Aartsen et al. (2018b). Table 5 lists all results for the investigated regions.

The best-fit parameter can yield insight into the source emission. However, as mentioned in Section 2 and Appendix A, the best-fit results and the resulting flux estimations are biased. The best-fit result of the number of neutrinos in the neutrino flare is $\hat{n}_S = 12^{+9}_{-7}$ with a spectral index of $\hat{\gamma} = 2.3 \pm 0.4$. This corresponds to an average flux of $\Phi^{\nu_\mu+\bar{\nu}_\mu}_{100\mathrm{TeV}} = 1.1^{+0.9}_{-0.8} \times 10^{-15}$ (TeV cm^2 s)$^{-1}$ in the energy range of 3.5 TeV to 213 TeV during the period of the neutrino flare. The corresponding single flavor neutrino and anti-neutrino fluence, the flux integrated over the flaring period ($\hat{\mu}_T - 2\hat{\sigma}_T$ to $\hat{\mu}_T + 2\hat{\sigma}_T$), is $J^{\nu_\mu+\bar{\nu}_\mu}_{100\mathrm{TeV}} = 1.2^{+1.0}_{-0.8} \times 10^{-8}$ (TeV cm^2)$^{-1}$. This flux estimation also agrees with Aartsen et al. (2018b), as shows the all-flavor neutrino flux (three times $\Phi^{\nu_\mu+\bar{\nu}_\mu}_{100\mathrm{TeV}}$) in Figure 4. In Appendix B, we compare the events contributing to the neutrino flare in this analysis and previous works and explain why the errors differ.

For transient emission, the lack of additional lower-energy neutrino emission (besides the reported local evidence associated with TXS 0506+056) can imply various scenarios. One is that neutrino flares occur rarely or might not necessarily be connected to the production sites of high-energy neutrinos. Similarly to Section 3.1, it could also indicate that these neutrino sources emit a very hard energy spectrum, for example, with $\gamma \leq 1$.

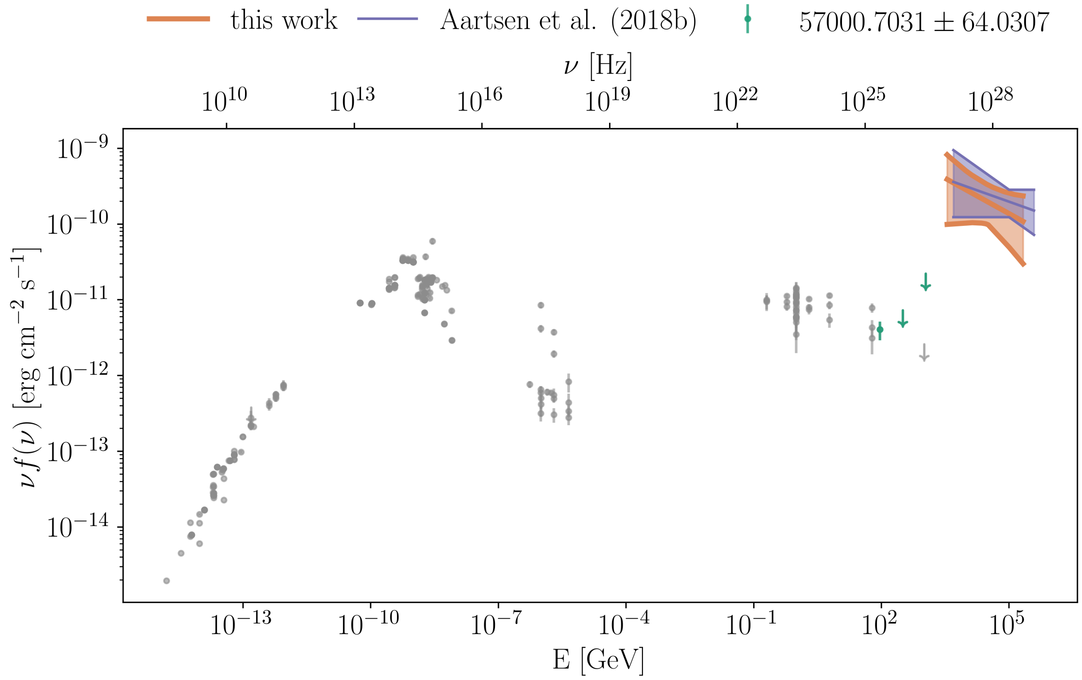

Figure 4. Spectral energy distribution of TXS 0506+056 in photons (grey dots) and neutrinos during the time of the neutrino flare (bands). The green dots (arrows) show gamma-ray emission (upper limits) during the time window of the neutrino flare detected by Fermi-LAT (Ackermann et al. 2012). This work's all-flavor neutrino flux during the flare (orange band, $3 \times \Phi^{\nu_\mu+\bar{\nu}_\mu}_{100\mathrm{TeV}}$) agrees with the all-flavor flux given in Aartsen et al. (2018b) (dark purple band). Data for the photon SED from Myers et al. (2003); Healey et al. (2007); Jackson et al. (2007); Nieppola et al. (2007); Condon et al. (1998); Wright et al. (1994); Planck Collaboration et al. (2011); Gregory et al. (1996); White & Becker (1992); Planck Collaboration et al. (2014, 2015); Wright et al. (2010); Bianchi et al. (2011); D'Elia et al. (2013); Evans et al. (2014); Voges et al. (1999); Boller et al. (2016); Abdo et al. (2010); Nolan et al. (2012); Acero et al. (2015); Bartoli et al. (2013); Giommi et al. (2018).

4. CONCLUSION

Our study focused on the origin of IceCube's highest energy events, or alert+ events, to identify potential sources of additional neutrino emission. To achieve this, we systematically scanned the 90% uncertainty contours of reconstructed alert+ events, with a resolution of 0.2 degrees, to determine the most significant source position. We assumed that the emission followed a power-law distribution, $\propto E^{-\gamma}$, with γ ranging from 1.5 to 4.

Our analysis found no evidence for continuous emission from a single source, as the data were consistent with the background assumption. Therefore, we placed a constraint on the overall combined flux from all positions, which was found to be 1.6% of the diffuse astrophysical neutrino flux observed by IceCube (for $\gamma = 2$). If we included the alert+ events in the analysis, we could constrain all expected emissions from their respective directions to no more than 4.5% of the diffuse astrophysical neutrino flux (for $\gamma = 2$). For a source spectral index similar to the diffuse astrophysical neutrino flux ($\gamma = 2.37$), we constrain the overall combined flux to be less than 1.5% (excluding the alert+ events) and less than 8% (including the alert+ events) of the diffuse astrophysical neutrino flux. This indicates that different source populations or states produce different neutrino spectra compared to one continuous power law.

Our investigation confirmed the neutrino flare associated with the blazar TXS 0506+056 as the most significant transient emission from all investigated positions, with a local significance of about 3σ. When we corrected for the look-elsewhere effect in this analysis, the global significance was 15.6%, consistent with the background expectation. The parameters of the neutrino flare in this study using recalibrated data agreed with previously published results. We identified a Gaussian time window with a center at 57001^{+38}_{-26} MJD, and a width of 64^{+35}_{-10} days as the best fit and estimated that 12^{+9}_{-6} neutrinos were detected during the flare with a best-fit spectral index of $\hat{\gamma} = 2.3 \pm 0.4$. This corresponds to a single flavor neutrino fluence of $J^{\nu_\mu+\bar{\nu}_\mu}_{100\mathrm{TeV}} = 1.2^{+1.0}_{-0.8} \times 10^{-8}$ (TeV cm^2)$^{-1}$ and an average flux of $\Phi^{\nu_\mu+\bar{\nu}_\mu}_{100\mathrm{TeV}} = 1.1^{+0.9}_{-0.8} \times 10^{-15}$ (TeV cm^2 s)$^{-1}$ during the $2\sigma_T$ time window. However, we find no other alert+ event with a similar local significance. TXS 0506+056 remains the only source candidate where we find a connection of a high-energy alert and a lower energetic neutrino emission.

For neither continuous nor transient emission did we find evidence of a lower energy neutrino component. This can be explained in various scenarios. One is a hard neutrino spectrum with $\gamma \leq 1$. In such a scenario, atmospheric background noise would dominate the lower energy range, while the higher energy range would yield single high-energy events. It could also be caused by a high-density source population as investigated in Abbasi et al. (2023b), where high-energy events are the result of fluctuations from a large population of sources with individually weak fluxes. In this case, the lower energy flux would still be too low to be detected. Our finding also suggests neutrino flares may be rare or produced at different sites than IceCube alert+ events or that there are sources mainly emitting high-energy neutrinos.

ACKNOWLEDGEMENTS

The IceCube Collaboration acknowledges significant contributions to this manuscript from Martina Karl. The authors gratefully acknowledge the support from the following agencies and institutions: USA – U.S. National Science Foundation-Office of Polar Programs, U.S. National Science Foundation-Physics Division, U.S. National Science Foundation-EPSCoR, U.S. National Science Foundation-Office of Advanced Cyberinfrastructure, Wisconsin Alumni Research Foundation, Center for High Throughput Computing (CHTC) at the University of Wisconsin–Madison, Open Science Grid (OSG), Partnership to Advance Throughput Computing (PATh), Advanced Cyberinfrastructure Coordination Ecosystem: Services & Support (ACCESS), Frontera computing project at the Texas Advanced Computing Center, U.S. Department of Energy-National Energy Research Scientific Computing Center, Particle astrophysics research computing center at the University of Maryland, Institute for Cyber-Enabled Research at Michigan State University, Astroparticle physics computational facility at Marquette University, NVIDIA Corporation, and Google Cloud Platform; Belgium – Funds for Scientific Research (FRS-FNRS and FWO), FWO Odysseus and Big Science programmes, and Belgian Federal Science Policy Office (Belspo); Germany – Bundesministerium für Bildung und Forschung (BMBF), Deutsche Forschungsgemeinschaft (DFG), Helmholtz Alliance for Astroparticle Physics (HAP), Initiative and Networking Fund of the Helmholtz Association, Deutsches Elektronen Synchrotron (DESY), and High Performance Computing cluster of the RWTH Aachen; Sweden – Swedish Research Council, Swedish Polar Research Secretariat, Swedish National Infrastructure for Computing (SNIC), and Knut and Alice Wallenberg Foundation; European Union – EGI Advanced Computing for research; Australia – Australian Research Council; Canada – Natural Sciences and Engineering Research Council of Canada, Calcul Québec, Compute Ontario, Canada Foundation for Innovation, WestGrid, and Digital Research Alliance of Canada; Denmark – Villum Fonden, Carlsberg Foundation, and European Commission; New Zealand – Marsden Fund; Japan – Japan Society for Promotion of Science (JSPS) and Institute for Global Prominent Research (IGPR) of Chiba University; Korea – National Research Foundation of Korea (NRF); Switzerland – Swiss National Science Foundation (SNSF).

APPENDIX

A. PARAMETER RECOVERY

When testing the method, as described in Section 2, with Monte Carlo simulations (Karl 2022), the best-fit number of signal neutrinos, n_S, and source spectral index, γ, show a bias compared to the true simulated source properties. For sources with simulated hard spectral indices (i.e., $\gamma = 2$), there is a tendency to fit slightly softer spectra and a slightly larger number of signal neutrinos. For example, simulating an average of 10 neutrinos with $\gamma = 2$ results in a mean best-fit of $\hat{n}_S = 16$ and $\hat{\gamma} = 2.25$. For simulated sources following softer spectral indices (i.e., $\gamma = 3$), the tendency is reversed to fitting slightly harder spectral indices and smaller numbers of signal neutrinos.

Several aspects influence this bias. One is a simplified spatial distribution in the form of a Rayleigh distribution (see Equation (3)). This is corrected using a kernel density estimation (KDE) approach, for example, in Abbasi et al. (2022a). However, the KDE approach is, so far, only feasible in the northern sky. Since we search for neutrino sources also from the southern sky, we chose the simplified method. Another aspect is that weak sources emitting only few neutrinos are not always found doing the position scan since background fluctuations can dominate these weak sources. For example, for a continuous emission over 11 years, the mean distance between the best-fit source position and the actual simulated source is smaller than 0.3 degrees for a flux resulting in 5 signal neutrinos on average. This also means that the best-fit n_S will be larger than 0 in many cases with no neutrino source since the algorithm will find the position with the largest background fluctuation. Hence, correcting this bias is not straightforward, and this analysis is mainly sensitive to strong neutrino sources.

For transient sources, the bias is smaller. In the same example as above, 10 neutrinos with $\gamma = 2$ emitted over a period of $\sigma_T \approx 55$ days are a much stronger signal compared to 10 neutrinos over 11 years. Hence in this specific case, the mean best-fit $\hat{n}_S = 12$ and the best-fit $\hat{\gamma} = 2.1$. However, we still face the case that background fluctuations can dominate weak neutrino emission (in the case of $\sigma_T \approx 55$ days, anything below 5 neutrinos is difficult), which makes correcting this bias challenging. We have decided not to include an, at best incomplete, correction in this work. For now, measurements of point-source fluxes are only possible with the KDE approach.

B. TRANSIENT SOURCES ANALYSIS

Figure 5 shows the p-value map of the scanned region around IceCube-170922A on the left. The most significant position is within 0.5° from TXS 0506+056. The right panel of Figure 5 shows a histogram of the angular distance of events from TXS 0506+056. There is a clustering of events around the source position. The signal events for this plot are simulated according to the best-fit result of the likelihood ratio test ($\hat{n}_S = 12$, $\hat{\gamma} = 2.3$). The background distribution is scrambled data in right ascension. The signal on top of the background flux matches the observed data.

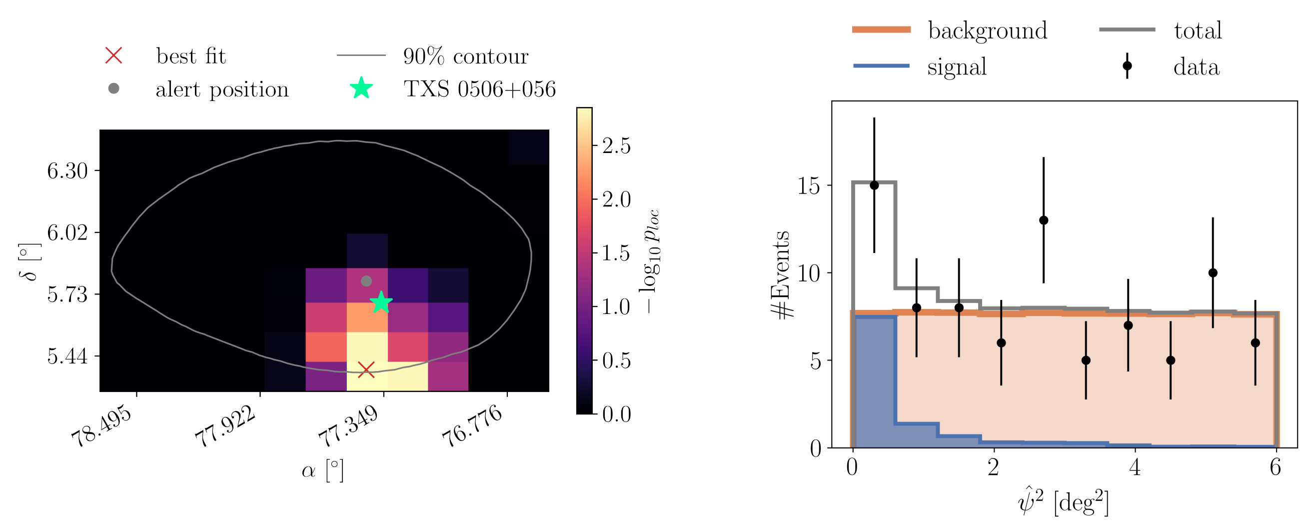

Figure 5. Left: P-value map of the alert region of IceCube-170922A. The grey dot indicates the reconstructed direction of IceCube-170922A, and the grey contour shows the 90% uncertainties of the reconstruction. The red cross marks the best-fit position of the position scan (0.6° from the reconstructed alert position). The star shows the location of TXS 0506+056. All black bins have p-values close to 1. **Right:** Number of events at binned squared angular distances, $\hat{\Psi}^2$, between TXS 0506+056 and the reconstructed event directions during the neutrino flare (57001 MJD $\pm\, 2 \times 64$ days). Scrambled data in right ascension provides the background (blue), and Monte Carlo simulations for the best-fitted flux ($n_S = 12$ and $\gamma = 2.31$) yield the signal (orange). The grey line combines the background with the signal and matches the data points (black). The data are shown with 68% uncertainties.

To determine the uncertainties of the best-fit values, we run a likelihood scan over the parameter space and use Wilk's theorem (Wilks 1938) to determine the 68% and 90% contours (see Figure 6). These contours are relevant for the two-dimensional uncertainties of the flux as in Figure 4. For the time, we determine the profiled change of the test statistic for different μ_T and σ_T. The best n_S and γ are fitted for each value. The 68% uncertainties determined by a profiled change of the test statistic are $\hat{\mu}_T = 57001^{+38}_{-26}$ MJD and $\hat{\sigma}_T = 64^{+35}_{-10}$ days. The one-dimensional errors for fluence, number of signal neutrinos, n_S, and spectral index γ, are determined with the profiled change of the test statistic where the mean flaring time and the flare width are kept fixed to the best-fit values. For the signal fluence the 68% uncertainties are are $J^{\nu_\mu+\bar{\nu}_\mu}_{100\mathrm{TeV}} = 1.2^{+1.0}_{-0.8} \times 10^{-8}$ (TeV cm^2)$^{-1}$ and for n_S and γ we get $\hat{n}_S = 12^{+9}_{-7}$ and $\hat{\gamma} = 2.3 \pm 0.4$.

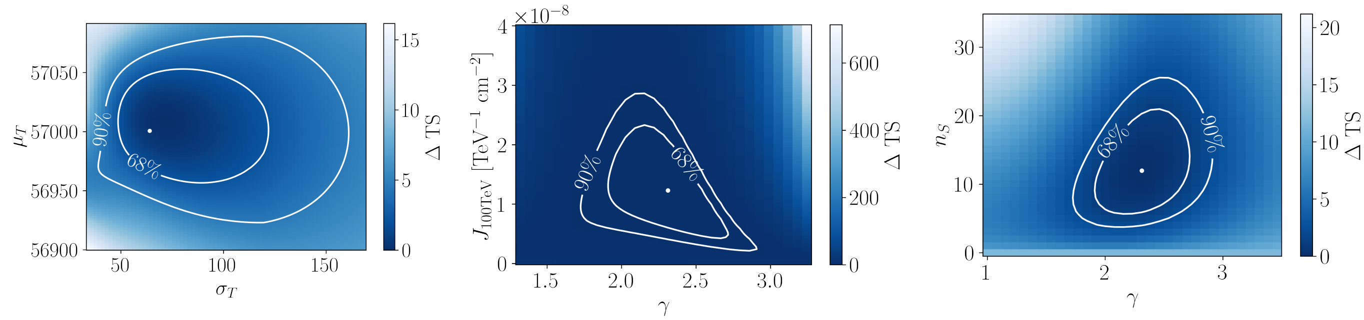

Figure 6. Change of the test statistic value for the different likelihood parameters. **Left:** Profiled change for different μ_T and σ_T. n_S and γ are optimized at each step. The 68% uncertainties are $\hat{\mu}_T = 57001^{+38}_{-26}$ MJD and $\hat{\sigma}_T = 64^{+35}_{-10}$ days. **Center:** Change when varying the signal fluence $J^{\nu_\mu+\bar{\nu}_\mu}_{100\text{TeV}}(n_S, \gamma)$. The 68% uncertainties on the fluence are $J^{\nu_\mu+\bar{\nu}_\mu}_{100\text{TeV}} = 1.2^{+1.0}_{-0.8} \times 10^{-8}$ (TeV cm^2)$^{-1}$. **Right:** Variation when changing n_S and γ. The 68% uncertainties are $\hat{n}_S = 12^{+9}_{-7}$ and $\hat{\gamma} = 2.3 \pm 0.4$.

Table 2. Left: Top 14 events with the strongest contribution to the neutrino flare of TXS 0506+056, sorted by significance. **Right:** The same events in the data sample published in Abbasi et al. (2021b). The last row states the ranking of the contribution in previous analyses. The data set used in this work has improved directional and energy reconstruction. Some events have shifted in position and have slightly different energies.

MJD	This work RA (deg)	Dec (deg)	σ (deg)	$\log_{10}(E/\text{GeV})$	Abbasi et al. (2021b) RA (deg)	Dec (deg)	σ (deg)	$\log_{10}(E/\text{GeV})$	Ranking
56940.9084	77.36	5.42	0.20	3.81	77.35	5.42	0.20	3.97	1
57009.5301	77.36	5.53	0.34	3.85	77.32	5.50	0.34	3.91	2
56973.3971	77.03	5.01	0.39	3.61	77.05	5.05	0.40	3.71	12
57112.6530	77.39	5.32	0.20	3.23	77.43	5.34	1.09	3.46	7
57072.2088	77.13	5.04	0.42	3.50	76.35	5.22	0.36	3.43	9
56981.1313	76.20	6.13	0.63	4.03	76.16	6.19	0.43	4.13	5
57089.4395	77.67	5.91	0.20	3.62	77.71	5.90	0.20	3.69	3
56927.8601	77.43	4.93	0.39	3.46	77.39	4.93	0.33	3.53	13
56955.7917	77.61	5.58	0.51	2.99	77.60	5.56	0.48	3.09	6
57072.9895	76.05	6.80	1.97	4.09	76.35	5.22	0.36	4.17	4
56940.5215	77.82	5.79	0.44	2.80	–	–	–	–	–
57031.8224	77.64	4.61	0.76	2.96	–	–	–	–	–
56937.8189	77.77	6.29	0.63	2.98	77.75	6.23	0.63	2.91	11
56983.2476	77.47	6.80	0.92	3.09	–	–	–	–	–

Table 2 lists the top 14 contributing events to the neutrino flare, sorted by their S_i/B_i value multiplied by S_T. We compare this with a previous data sample (Abbasi et al. 2021b) (for events also included in that sample) to emphasize how the updated photomultiplier calibration affects the reconstructed direction, angular error, and energy.

The improved directional and energy reconstruction has changed the contributing events compared to previous analyses (Aartsen et al. 2018b; Abbasi et al. 2021b). Most of the significance is caused by the two most contributing events, which remain the same (see also Karl (2022)). However, their position is shifted, and their energy is changed. For the remaining events, the contributing order has changed, or the events themselves differ. Figure 7 shows the position and energy of the 14 most contributing events to the neutrino flare from the previous data set (left) and the improved data used in this work (right). The event with the largest error region ($\sigma = 1.9°$) on the right panel is also included in the left panel. However, the uncertainty was underestimated in the previous data sample ($\sigma = 0.36°$), and its position has shifted.

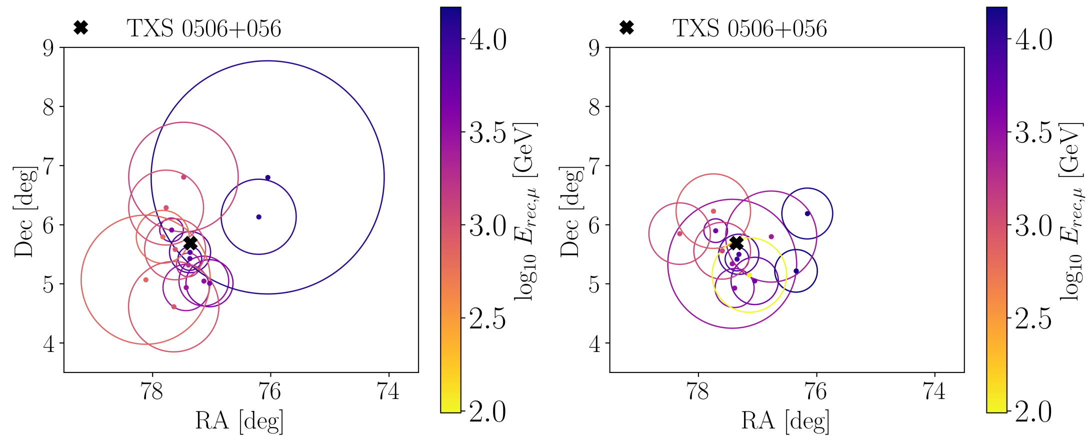

Figure 7. Position and energy (color) of the 14 most contributing events to the TXS 0506+056 neutrino flare. The circles show the uncertainty of the directional reconstruction, σ_i. **Left:** The 14 most contributing events from the data sample used in this work (see Table 2). **Right:** The 14 most contributing events from the old data sample (Abbasi et al. 2021b).

C. ICECUBE ALERT+ EVENTS

Table 3. All alert events (track name starting with "IC") and high-energy tracks (track name starting with "DIF" (selected from Abbasi et al. (2022b)), "EHE" (extremely-high-energy), or "HESE" (high-energy-starting event)) investigated in this work. The track name includes the time of detection in the format yymmdd. In the case of alert events, the letter "A" or "B" is used to distinguish events detected on the same day. The time is the detection time in MJD, and R.A. and Dec list the best reconstruction coordinates with 90% confidence level uncertainties.

Index	Track Name	Time [MJD]	R.A. [deg]	Dec [deg]
1	DIF090813	55056.6983	$29.51^{+0.40}_{-0.38}$	$1.23^{+0.18}_{-0.22}$
2	DIF091106	55141.1275	$298.21^{+0.53}_{-0.57}$	$11.74^{+0.32}_{-0.38}$
3	DIF100608	55355.4872	$344.93^{+3.39}_{-2.90}$	$23.58^{+2.31}_{-4.13}$
4	DIF100623	55370.7355	$141.25^{+0.46}_{-0.45}$	$47.80^{+0.56}_{-0.48}$
5	DIF100710	55387.5362	$306.96^{+2.70}_{-2.28}$	$21.00^{+2.25}_{-1.56}$
6	DIF100925	55464.8959	$266.29^{+0.58}_{-0.62}$	$13.40^{+0.52}_{-0.45}$
7	DIF101009	55478.3806	$331.09^{+0.56}_{-0.72}$	$11.10^{+0.48}_{-0.58}$
8	DIF101028	55497.3033	$88.68^{+0.54}_{-0.55}$	$0.46^{+0.33}_{-0.27}$
9	HESE101112	55512.5516	$110.56^{+0.80}_{-0.37}$	$-0.37^{+0.48}_{-0.65}$
10	DIF101113	55513.5995	$285.95^{+1.29}_{-1.50}$	$3.15^{+0.70}_{-0.63}$
11	DIF110128	55589.5628	$307.53^{+0.82}_{-0.81}$	$1.19^{+0.35}_{-0.32}$
12	EHE110304	55624.9548	$116.37^{+0.73}_{-0.73}$	$-10.72^{+0.57}_{-0.65}$
13	IC110514A	55695.0642	$138.47^{+6.68}_{-3.78}$	$-1.94^{+0.97}_{-1.12}$
14	DIF110521	55702.7666	$235.13^{+2.70}_{-1.76}$	$20.30^{+1.00}_{-1.43}$
15	IC110610A	55722.4261	$272.55^{+1.67}_{-2.42}$	$35.64^{+1.30}_{-1.05}$
16	IC110714A	55756.1130	$68.20^{+0.31}_{-1.10}$	$40.67^{+0.44}_{-0.44}$
17	DIF110722	55764.2196	$315.66^{+5.91}_{-5.35}$	$5.29^{+4.85}_{-4.72}$
18	IC110902A	55806.0922	$9.76^{+2.85}_{-1.32}$	$7.59^{+0.87}_{-0.86}$
19	IC110907A	55811.7946	$196.08^{+3.92}_{-2.68}$	$9.40^{+1.56}_{-1.05}$
20	DIF110930	55834.4451	$266.48^{+2.09}_{-1.55}$	$-4.41^{+0.59}_{-0.86}$
21	DIF111201	55896.8575	$222.87^{+1.95}_{-7.73}$	$1.87^{+1.25}_{-1.18}$

Continued on next page

Table 3 – continued from previous page

Index	Track Name	Time [MJD]	R.A. [deg]	Dec [deg]
22	IC111216A	55911.2769	$36.74^{+1.80}_{-2.24}$	$18.88^{+2.46}_{-2.82}$
23	IC120301A	55987.8069	$237.96^{+0.53}_{-0.61}$	$18.76^{+0.47}_{-0.51}$
24	IC120515A	56062.9590	$198.94^{+1.71}_{-1.41}$	$32.00^{+0.97}_{-1.09}$
25	IC120523A	56070.5743	$171.08^{+0.66}_{-1.41}$	$26.44^{+0.46}_{-0.37}$
26	IC120807A	56146.2071	$330.07^{+0.84}_{-0.83}$	$1.42^{+0.59}_{-0.45}$
27	IC120916A	56186.3053	$182.24^{+1.36}_{-1.71}$	$3.88^{+0.68}_{-0.82}$
28	IC120922A	56192.5493	$70.62^{+1.49}_{-1.27}$	$19.79^{+0.91}_{-0.71}$
29	IC121011A	56211.7709	$205.14^{+0.66}_{-0.71}$	$-2.28^{+0.53}_{-0.56}$
30	IC121026A	56226.5995	$169.80^{+1.32}_{-1.40}$	$27.91^{+0.85}_{-0.88}$
31	IC130127A	56319.2800	$352.97^{+1.32}_{-1.01}$	$-1.98^{+0.97}_{-0.89}$
32	IC130408A	56390.1888	$167.83^{+2.63}_{-3.96}$	$20.66^{+1.28}_{-0.99}$
33	IC130627A	56470.1104	$93.74^{+1.01}_{-1.15}$	$14.17^{+1.23}_{-1.04}$
34	DIF130817	56521.8320	$224.89^{+0.87}_{-1.19}$	$-4.44^{+1.21}_{-0.94}$
35	IC130907A	56542.7931	$130.17^{+0.48}_{-0.31}$	$-10.54^{+0.26}_{-0.30}$
36	IC131014A	56579.9092	$32.92^{+0.87}_{-0.71}$	$10.28^{+0.41}_{-0.57}$
37	IC131023A	56588.5585	$301.90^{+1.02}_{-1.05}$	$11.61^{+1.14}_{-1.30}$
38	IC131124A	56620.1451	$285.16^{+2.20}_{-1.54}$	$19.47^{+1.43}_{-1.46}$
39	IC131204A	56630.4701	$288.98^{+1.10}_{-0.83}$	$-14.21^{+0.77}_{-1.31}$
40	IC140101A	56658.4039	$192.26^{+2.07}_{-2.37}$	$-2.69^{+1.01}_{-0.71}$
41	IC140108A	56665.3079	$344.66^{+0.53}_{-0.48}$	$1.57^{+0.37}_{-0.34}$
42	IC140109A	56666.5030	$293.12^{+0.79}_{-1.19}$	$33.02^{+0.45}_{-0.53}$
43	IC140203A	56691.7851	$349.58^{+2.64}_{-2.54}$	$-13.55^{+1.14}_{-1.74}$
44	DIF140522	56799.9614	$349.39^{+2.89}_{-4.12}$	$18.05^{+1.94}_{-1.80}$
45	IC140609A	56817.6364	$106.26^{+2.68}_{-2.15}$	$1.31^{+1.04}_{-0.86}$
46	IC140611A	56819.2044	$110.65^{+0.53}_{-0.61}$	$11.45^{+0.19}_{-0.19}$
47	IC140705A	56843.6687	$25.88^{+1.85}_{-2.98}$	$2.54^{+1.79}_{-1.76}$
48	IC140923A	56923.7211	$169.72^{+0.70}_{-0.84}$	$-1.60^{+0.52}_{-0.30}$
49	IC140927A	56927.1608	$50.89^{+3.91}_{-5.14}$	$-0.63^{+1.49}_{-1.42}$
50	IC150127A	57049.4813	$100.37^{+1.36}_{-1.62}$	$4.59^{+0.79}_{-0.67}$
51	IC150515A	57157.9416	$91.49^{+0.93}_{-0.74}$	$12.14^{+0.53}_{-0.50}$
52	IC150714A	57217.9097	$326.29^{+1.50}_{-1.31}$	$26.36^{+1.89}_{-2.19}$
53	IC150812B	57246.7591	$328.27^{+0.75}_{-0.88}$	$6.17^{+0.48}_{-0.53}$
54	IC150831A	57265.2178	$54.76^{+0.92}_{-0.93}$	$34.00^{+1.14}_{-1.20}$
55	IC150904A	57269.7597	$133.77^{+0.53}_{-0.88}$	$28.08^{+0.51}_{-0.55}$
56	IC150919A	57284.2057	$279.54^{+1.75}_{-2.29}$	$30.35^{+2.18}_{-1.51}$
57	IC150923A	57288.0268	$103.23^{+0.70}_{-1.15}$	$3.96^{+0.60}_{-0.75}$
58	IC150926A	57291.9012	$194.55^{+0.79}_{-1.23}$	$-4.56^{+0.94}_{-0.63}$
59	IC151017A	57312.6757	$197.53^{+2.47}_{-2.72}$	$19.95^{+3.00}_{-2.29}$
60	IC151114A	57340.8735	$76.16^{+1.36}_{-1.37}$	$12.71^{+0.65}_{-0.72}$
61	IC151122A	57348.5316	$262.05^{+0.87}_{-1.06}$	$-2.24^{+0.64}_{-0.67}$
62	IC160104A	57391.4438	$79.41^{+0.83}_{-0.75}$	$5.00^{+0.87}_{-0.97}$
63	IC160128A	57415.1835	$263.76^{+1.10}_{-1.80}$	$-14.90^{+1.08}_{-1.20}$
64	IC160225A	57443.8804	$311.87^{+2.19}_{-1.77}$	$60.06^{+1.65}_{-1.38}$
65	IC160331A	57478.5652	$151.22^{+0.66}_{-0.66}$	$15.48^{+0.66}_{-0.73}$
66	IC160510A	57518.6640	$352.88^{+1.76}_{-1.45}$	$1.90^{+0.75}_{-0.67}$
67	EHE160731	57600.0799	$214.50^{+0.75}_{-0.75}$	$-0.33^{+0.75}_{-0.75}$
68	IC160806A	57606.5150	$122.78^{+0.88}_{-1.23}$	$-0.71^{+0.56}_{-0.56}$

Continued on next page

Table 3 – continued from previous page

Index	Track Name	Time [MJD]	R.A. [deg]	Dec [deg]
69	IC160814A	57614.9069	$200.04^{+3.12}_{-2.68}$	$-32.13^{+1.74}_{-1.25}$
70	IC160924A	57655.7411	$241.13^{+4.92}_{-5.89}$	$1.34^{+3.40}_{-2.79}$
71	IC161001A	57662.4392	$192.57^{+2.50}_{-2.07}$	$37.12^{+1.51}_{-2.48}$
72	DIF161011	57672.0796	$26.38^{+0.66}_{-0.66}$	$9.55^{+0.66}_{-0.66}$
73	IC161012A	57673.6126	$190.06^{+2.20}_{-4.04}$	$-7.48^{+2.18}_{-2.99}$
74	IC161117A	57709.3320	$78.66^{+1.85}_{-1.93}$	$1.60^{+1.91}_{-1.79}$
75	IC161210A	57732.8380	$46.36^{+2.38}_{-0.92}$	$15.25^{+0.93}_{-1.08}$
76	IC170105A	57758.1419	$309.95^{+5.01}_{-7.56}$	$8.16^{+2.00}_{-3.34}$
77	IC170321A	57833.3141	$98.26^{+1.32}_{-0.92}$	$-15.06^{+1.04}_{-1.20}$
78	IC170514B	57887.3002	$227.37^{+1.23}_{-1.10}$	$30.65^{+1.40}_{-0.99}$
79	IC170626A	57930.5193	$280.99^{+3.03}_{-1.63}$	$8.80^{+1.13}_{-0.90}$
80	IC170704A	57938.2926	$230.45^{+1.67}_{-1.71}$	$23.36^{+1.10}_{-0.89}$
81	IC170717A	57951.8177	$208.39^{+1.67}_{-1.19}$	$25.16^{+1.41}_{-1.35}$
82	IC170803A	57968.0838	$1.10^{+4.48}_{-1.76}$	$4.63^{+0.41}_{-0.41}$
83	IC170809A	57974.5971	$21.27^{+0.75}_{-1.06}$	$-2.28^{+0.60}_{-0.67}$
84	IC170824A	57989.5538	$41.92^{+3.04}_{-3.56}$	$12.37^{+1.45}_{-1.30}$
85	IC170922A	58018.8712	$77.43^{+1.14}_{-0.75}$	$5.79^{+0.64}_{-0.41}$
86	IC170923A	58019.0213	$173.45^{+2.38}_{-2.55}$	$-2.54^{+0.90}_{-1.30}$
87	IC171015A	58041.0656	$162.91^{+2.98}_{-1.72}$	$-15.48^{+1.62}_{-1.99}$
88	IC171106A	58063.7775	$340.14^{+0.61}_{-0.62}$	$7.44^{+0.31}_{-0.26}$
89	IC180123A	58141.6771	$77.12^{+2.51}_{-2.90}$	$8.01^{+0.41}_{-0.49}$
90	IC180410A	58218.7768	$218.50^{+0.79}_{-1.28}$	$0.56^{+0.75}_{-0.71}$
91	IC180417A	58225.2785	$305.73^{+3.60}_{-1.58}$	$-4.41^{+0.68}_{-0.74}$
92	IC180908A	58369.8330	$144.98^{+1.49}_{-2.20}$	$-2.39^{+1.16}_{-1.12}$
93	IC181023A	58414.6927	$270.18^{+1.89}_{-1.72}$	$-8.42^{+1.13}_{-1.55}$
94	IC181120A	58442.7087	$25.71^{+5.54}_{-5.28}$	$11.72^{+2.41}_{-4.50}$
95	IC181121A	58443.5800	$132.19^{+7.34}_{-6.99}$	$32.93^{+4.19}_{-3.57}$
96	IC190124A	58507.1555	$307.44^{+0.53}_{-1.14}$	$-32.22^{+0.96}_{-0.31}$
97	IC190214A	58528.6727	$228.25^{+0.79}_{-0.53}$	$-4.14^{+0.37}_{-0.30}$
98	IC190221A	58535.3512	$268.59^{+1.41}_{-1.58}$	$-17.00^{+1.25}_{-0.50}$
99	IC190503A	58606.7244	$120.19^{+0.66}_{-0.66}$	$6.43^{+0.68}_{-0.75}$
100	IC190515A	58618.4506	$127.88^{+0.79}_{-0.83}$	$12.60^{+0.49}_{-0.46}$
101	IC190613A	58647.8294	$312.19^{+0.66}_{-0.79}$	$26.57^{+0.75}_{-0.71}$
102	IC190619A	58653.5516	$343.52^{+4.13}_{-3.16}$	$10.28^{+2.01}_{-2.76}$
103	IC190730A	58694.8685	$226.14^{+1.28}_{-1.97}$	$10.77^{+1.03}_{-1.18}$
104	IC190922A	58748.4047	$167.30^{+2.81}_{-2.72}$	$-22.27^{+3.39}_{-3.30}$
105	IC190922B	58748.9611	$5.71^{+1.19}_{-1.27}$	$-1.53^{+0.90}_{-0.78}$
106	IC191001A	58757.8398	$313.99^{+6.94}_{-2.46}$	$12.79^{+1.65}_{-1.64}$
107	IC191119A	58806.0427	$229.31^{+5.49}_{-4.97}$	$3.77^{+2.47}_{-2.24}$
108	IC200109A	58857.9873	$165.45^{+3.61}_{-4.39}$	$11.80^{+1.18}_{-1.30}$
109	IC200530A	58999.3295	$255.37^{+2.46}_{-2.55}$	$26.61^{+2.32}_{-3.25}$
110	IC200615A	59015.6176	$142.95^{+1.15}_{-1.40}$	$3.66^{+1.16}_{-1.01}$
111	IC200926A	59118.3293	$96.46^{+0.70}_{-0.53}$	$-4.33^{+0.60}_{-0.75}$
112	IC200929A	59121.7421	$29.53^{+0.53}_{-0.53}$	$3.47^{+0.71}_{-0.34}$
113	IC201007A	59129.9179	$265.17^{+0.48}_{-0.49}$	$5.34^{+0.30}_{-0.19}$
114	IC201114A	59167.6288	$105.73^{+0.93}_{-1.27}$	$5.87^{+1.01}_{-1.05}$
115	IC201115A	59168.0885	$195.12^{+1.23}_{-1.45}$	$1.38^{+1.27}_{-1.08}$

Continued on next page

Table 3 – continued from previous page

Index	Track Name	Time [MJD]	R.A. [deg]	Dec [deg]
116	IC201130A	59183.8485	$30.54^{+1.10}_{-1.27}$	$-12.10^{+1.14}_{-1.11}$
117	IC201209A	59192.4276	$6.86^{+1.01}_{-1.19}$	$-9.25^{+0.94}_{-1.10}$
118	IC201221A	59204.5256	$261.69^{+2.28}_{-2.46}$	$41.81^{+1.25}_{-1.14}$
119	IC201222A	59205.0391	$206.37^{+0.88}_{-0.75}$	$13.44^{+0.54}_{-0.35}$
120	IC210210A	59255.4958	$206.06^{+1.40}_{-0.95}$	$4.78^{+0.62}_{-0.56}$
121	IC210811A	59437.0852	$270.79^{+1.07}_{-1.08}$	$25.28^{+0.79}_{-0.84}$
122	IC210922A	59479.7620	$60.73^{+0.88}_{-0.61}$	$-4.18^{+0.37}_{-0.53}$

D. RESULT TABLES

Table 4. Results of the individual time-integrated analysis sorted by significance. The first column contains the index of the alert+ event as in Table 3. The two following columns list the best-fit position of this work. The fourth and fifth columns contain the best-fit parameter of the likelihood optimization $\hat{n}_s$ and $\hat{\gamma}$. The sixth column shows the local p-values, and the seventh column the 90% confidence level upper flux limits. The central 90% quantiles of neutrino energies of the detected simulated events for computing the flux limit are listed in columns eight and nine. They define the range in which the flux limit is valid. The global p-value for the time-integrated single-source search is 0.98.

Index	R.A. [deg]	Dec [deg]	$\hat{n}_S$	$\hat{\gamma}$	p_{local}	$\Phi_{90\%100\mathrm{TeV}}$ $[\mathrm{TeV\ cm^2\ s}]^{-1}$	$E_{\nu,\Phi,\min}$ [TeV]	$E_{\nu,\Phi,\max}$ [TeV]
13	137.87	-2.69	37.50	3.20	0.02	6.88×10^{-17}	0.9	483.1
106	318.48	11.88	13.38	2.08	0.03	9.00×10^{-17}	0.7	132.7
14	237.00	19.41	46.18	4.00	0.03	9.20×10^{-17}	0.7	88.3
2	298.74	11.74	38.86	4.00	0.04	8.95×10^{-17}	0.7	134.0
83	22.02	-2.13	28.76	2.93	0.04	5.00×10^{-17}	0.9	439.5
54	54.99	33.66	34.34	4.00	0.04	5.58×10^{-17}	0.7	50.8
16	68.36	40.82	4.48	1.71	0.05	7.31×10^{-17}	0.7	40.8
50	50.69	-0.44	43.72	4.00	0.06	5.77×10^{-17}	0.8	380.2
74	79.40	2.75	20.01	2.49	0.06	6.35×10^{-17}	0.8	293.8
10	284.83	3.32	16.71	2.38	0.07	7.66×10^{-17}	0.8	286.4
60	75.38	12.87	13.39	2.17	0.07	4.77×10^{-17}	0.7	118.6
23	237.76	19.08	37.66	4.00	0.07	6.31×10^{-17}	0.7	95.1
44	349.58	-13.17	12.27	2.64	0.07	6.17×10^{-17}	17.3	5093.3
25	171.74	26.44	11.18	2.31	0.07	6.01×10^{-17}	0.7	67.3
72	26.38	9.55	9.84	2.13	0.08	2.15×10^{-16}	0.8	158.1
45	350.01	19.02	40.34	3.91	0.10	7.68×10^{-17}	0.7	101.2
40	190.68	-2.35	26.39	4.00	0.11	4.11×10^{-17}	0.9	462.4
90	218.32	-0.15	32.53	3.49	0.11	4.22×10^{-17}	0.8	368.1
11	307.86	1.36	11.50	2.42	0.14	3.24×10^{-17}	0.8	353.2
93	269.42	-7.48	15.52	2.95	0.15	8.71×10^{-17}	2.2	2118.4
65	151.55	15.98	30.25	3.05	0.16	5.88×10^{-17}	0.7	105.0
77	99.20	-15.86	11.40	3.81	0.16	2.11×10^{-16}	22.7	6823.4
84	43.34	12.18	40.03	3.49	0.16	7.54×10^{-17}	0.7	131.2
85	77.43	5.38	16.73	2.54	0.17	4.18×10^{-17}	0.8	237.1
99	120.35	6.05	24.65	2.81	0.20	4.68×10^{-17}	0.8	223.4
55	133.77	27.71	22.04	4.00	0.20	3.85×10^{-17}	0.7	64.4
120	206.26	4.41	26.47	2.89	0.20	3.79×10^{-17}	0.8	265.5
4	141.25	47.32	17.24	2.61	0.21	7.67×10^{-17}	0.7	32.4
9	111.36	-0.37	25.89	4.00	0.21	2.89×10^{-17}	0.8	371.5
81	208.19	25.69	5.14	1.86	0.22	5.56×10^{-17}	0.7	65.9
28	70.62	19.43	8.08	2.09	0.22	4.92×10^{-17}	0.7	86.5
15	273.27	36.20	22.40	2.72	0.22	6.14×10^{-17}	0.7	43.9
30	171.12	27.73	32.96	3.94	0.23	5.37×10^{-17}	0.7	62.2
31	353.91	-1.20	20.58	2.65	0.24	3.11×10^{-17}	0.9	394.5
18	9.38	7.59	5.54	2.09	0.24	4.38×10^{-17}	0.8	181.1
115	194.76	2.47	17.33	2.48	0.26	2.81×10^{-17}	0.8	300.6

Continued on next page

Table 4 – continued from previous page

Index	R.A. [deg]	Dec [deg]	$\hat{n}_S$	$\hat{\gamma}$	p_{local}	$\Phi_{90\%100\mathrm{TeV}}$ [TeV cm^2 s]$^{-1}$	$E_{\nu,\Phi,\min}$ [TeV]	$E_{\nu,\Phi,\max}$ [TeV]
33	93.74	14.17	18.68	2.58	0.26	3.76×10^{-17}	0.7	116.7
113	265.17	5.15	21.84	4.00	0.28	4.00×10^{-17}	0.8	248.3
47	27.54	2.74	36.77	3.79	0.28	3.52×10^{-17}	0.8	293.8
34	225.59	-4.09	14.38	2.78	0.30	3.24×10^{-17}	1.0	642.7
119	206.90	13.27	20.54	3.16	0.30	3.12×10^{-17}	0.7	118.6
112	29.35	3.30	22.47	3.12	0.30	3.70×10^{-17}	0.8	281.2
114	104.46	6.38	28.34	3.01	0.30	2.82×10^{-17}	0.8	224.4
94	26.90	7.81	47.41	4.00	0.30	7.00×10^{-17}	0.8	170.6
7	330.73	11.10	21.11	2.90	0.31	3.57×10^{-17}	0.7	134.0
56	277.48	29.41	25.41	2.83	0.32	2.86×10^{-17}	0.7	55.0
75	46.95	15.99	32.99	3.15	0.32	4.65×10^{-17}	0.7	106.7
59	195.23	20.14	8.95	2.09	0.33	6.66×10^{-17}	0.7	83.0
79	283.21	9.37	32.19	3.43	0.33	5.19×10^{-17}	0.8	167.1
78	227.78	30.25	28.65	4.00	0.33	6.23×10^{-17}	0.7	54.3
122	60.27	-3.99	6.55	4.00	0.34	5.41×10^{-17}	1.0	619.4
52	91.86	12.32	23.31	3.25	0.34	3.58×10^{-17}	0.7	130.0
86	171.49	-2.36	8.32	2.19	0.34	3.72×10^{-17}	0.9	467.7
49	168.88	-1.43	20.41	4.00	0.35	2.03×10^{-17}	0.9	409.3
109	255.82	26.80	26.23	2.85	0.36	2.66×10^{-17}	0.7	67.8
88	340.75	7.44	19.33	4.00	0.37	8.03×10^{-17}	0.8	187.5
70	237.60	1.14	41.83	4.00	0.38	4.43×10^{-17}	0.8	334.2
87	164.10	-14.76	11.78	3.90	0.39	5.17×10^{-17}	20.7	6368.0
46	105.48	1.66	25.18	2.74	0.40	1.73×10^{-16}	0.8	320.6
102	343.52	9.69	42.18	3.38	0.40	2.69×10^{-17}	0.7	158.9
66	354.25	1.40	27.02	4.00	0.41	2.40×10^{-17}	0.8	338.1
92	144.38	-3.14	18.45	4.00	0.42	2.90×10^{-17}	0.9	517.6
100	128.67	12.76	5.42	2.18	0.43	3.28×10^{-17}	0.7	123.0
110	143.14	3.32	21.32	2.82	0.46	3.36×10^{-17}	0.8	281.2
97	228.84	-3.96	6.79	4.00	0.46	3.30×10^{-17}	1.0	620.9
91	304.94	-4.97	12.09	4.00	0.47	1.34×10^{-16}	1.1	871.0
63	264.13	-15.07	8.15	3.88	0.47	4.46×10^{-17}	21.1	6295.1
101	312.19	25.86	7.93	2.24	0.47	1.57×10^{-16}	0.7	68.9
98	269.80	-16.11	9.81	3.67	0.47	4.83×10^{-17}	23.3	6982.3
108	167.45	12.39	31.98	3.15	0.48	5.15×10^{-17}	0.7	127.1
5	306.96	19.44	15.41	2.38	0.49	4.10×10^{-17}	0.7	86.9
26	329.57	1.82	19.70	4.00	0.49	1.85×10^{-17}	0.8	308.3
68	122.25	-0.34	18.24	3.96	0.51	2.00×10^{-17}	0.8	380.2
37	301.20	10.50	5.10	2.17	0.51	3.23×10^{-17}	0.7	140.9
41	344.50	1.94	4.08	2.21	0.52	2.54×10^{-17}	0.8	309.0
27	180.72	3.55	19.65	3.14	0.55	2.43×10^{-17}	0.8	291.7
69	200.71	-31.94	9.69	3.55	0.57	2.51×10^{-17}	61.9	11967.4
117	5.67	-9.06	7.22	2.95	0.57	4.89×10^{-16}	5.5	2944.4
51	99.29	4.59	23.19	3.09	0.57	6.52×10^{-17}	0.8	251.2
6	266.87	13.40	9.33	2.66	0.57	3.08×10^{-17}	0.7	118.3
39	289.16	-14.21	6.66	3.15	0.59	9.48×10^{-17}	19.1	5701.6
64	312.60	59.86	9.68	2.06	0.59	8.38×10^{-17}	0.6	23.8

Continued on next page

Table 4 – continued from previous page

Index	R.A. [deg]	Dec [deg]	$\hat{n}_S$	$\hat{\gamma}$	p_{local}	$\Phi_{90\%100\mathrm{TeV}}$ [TeV cm^2 s]$^{-1}$	$E_{\nu,\Phi,\min}$ [TeV]	$E_{\nu,\Phi,\max}$ [TeV]
73	187.17	-6.89	9.57	2.26	0.61	4.64×10^{-17}	1.6	1706.1
25	199.80	32.58	16.22	2.75	0.61	7.43×10^{-17}	0.7	51.9
80	230.24	23.91	16.44	2.66	0.62	4.83×10^{-17}	0.7	64.9
105	4.80	-1.92	16.74	2.82	0.62	2.82×10^{-17}	0.9	424.6
61	261.34	-2.58	9.54	2.82	0.67	2.46×10^{-17}	0.9	460.3
104	166.88	-20.47	5.88	2.16	0.68	2.72×10^{-17}	36.8	8851.2
22	37.34	18.88	27.49	3.83	0.70	2.80×10^{-16}	0.7	101.9
32	169.25	20.84	22.64	2.87	0.71	4.67×10^{-17}	0.7	79.4
107	233.04	3.02	35.13	3.54	0.73	4.45×10^{-17}	0.8	281.8
118	263.47	42.52	6.25	1.99	0.74	4.06×10^{-17}	0.7	40.2
58	193.67	-3.81	6.84	4.00	0.74	3.21×10^{-17}	1.0	588.8
20	266.48	-5.10	9.66	3.55	0.74	6.92×10^{-17}	1.1	948.4
116	30.72	-11.91	6.42	3.38	0.76	3.81×10^{-17}	13.6	4786.3
12	115.64	-10.72	1.53	2.35	0.76	4.62×10^{-17}	10.7	4064.4
95	127.53	35.53	26.45	2.65	0.77	9.04×10^{-17}	0.7	47.3
3	347.90	22.20	33.17	4.00	0.79	8.66×10^{-17}	0.7	78.2
121	270.36	25.11	13.05	4.00	0.79	4.86×10^{-17}	0.7	68.2
38	284.97	19.11	19.88	4.00	0.80	3.57×10^{-16}	0.7	94.0
52	326.72	27.30	7.78	2.44	0.80	4.65×10^{-17}	0.7	62.8
89	79.63	8.01	19.75	4.00	0.81	4.12×10^{-17}	0.8	166.7
96	307.97	-32.03	2.48	2.49	0.81	3.93×10^{-17}	61.5	12416.5
47	110.83	11.45	4.77	3.57	0.82	6.09×10^{-17}	0.7	136.8
57	103.41	3.96	2.01	2.14	0.82	3.55×10^{-17}	0.8	281.8
62	79.41	5.00	12.34	3.04	0.83	2.81×10^{-17}	0.8	260.0
42	293.71	33.32	7.76	2.89	0.83	2.83×10^{-17}	0.7	48.3
82	4.61	4.36	16.46	4.00	0.85	3.26×10^{-17}	0.8	272.3
19	194.36	9.59	25.50	4.00	0.86	4.15×10^{-17}	0.7	158.1
103	225.75	10.77	12.59	2.88	0.88	2.55×10^{-17}	0.7	141.6
36	33.79	10.09	2.16	2.01	0.91	4.01×10^{-17}	0.8	158.9
76	310.75	9.07	9.19	2.17	0.93	3.58×10^{-17}	0.7	165.6
21	222.47	0.89	17.33	3.34	0.94	2.55×10^{-17}	0.8	342.8
67	214.31	-0.89	8.92	3.32	0.94	5.71×10^{-17}	0.8	363.1
71	193.07	37.50	14.94	3.19	0.94	3.45×10^{-17}	0.7	42.6
17	314.47	8.39	30.90	3.32	0.99	7.36×10^{-17}	0.8	171.0
111	96.46	-5.08	0.55	3.35	1.00	2.74×10^{-17}	1.1	924.7
53	327.74	5.82	1.69	3.75	1.00	4.50×10^{-17}	0.8	229.1
29	204.43	-2.47	0.00	2.56	1.00	1.87×10^{-17}	0.9	465.6
1	29.32	1.12	0.00	2.83	1.00	1.83×10^{-17}	0.8	333.4
8	88.31	0.33	0.00	3.20	1.00	2.04×10^{-17}	0.8	376.7
35	130.01	-10.69	0.00	1.50	1.00	5.02×10^{-17}	10.6	4083.2

Table 5. Results of the time-dependent analysis sorted by significance. The first column contains the alert+ index as in Table 3. The next two columns list the best-fit position. The fourth and fifth columns contain the best-fit parameter of the likelihood optimization n_s and γ. The sixth and seventh column list the best-fit results for the Gaussian time window with mean μ_T and width σ_t. The last column shows the local p-values. The global p-value for the time-dependent analysis is 0.156.

Index	R.A. [deg]	Dec [deg]	$\hat{n}_S$	$\hat{\gamma}$	$\hat{\mu}_T$	$\hat{\sigma}_T$	p_{local}
85	77.43	5.38	11.98	2.31	57001	64	1.4×10^{-3}
107	227.72	5.10	9.48	2.38	57774	9	1.6×10^{-2}
17	318.42	1.75	10.41	2.45	57008	20	1.7×10^{-2}
60	75.77	13.20	5.19	2.07	58155	10	1.9×10^{-2}
33	93.74	14.35	14.45	2.96	57078	39	2.1×10^{-2}
30	169.60	28.76	8.52	3.04	56153	5	2.5×10^{-2}
83	21.27	−2.95	18.44	2.90	57186	236	3.4×10^{-2}
120	206.26	4.41	19.76	3.02	57427	103	5.1×10^{-2}
99	120.19	5.87	12.71	2.68	56267	51	5.5×10^{-2}
87	164.10	−17.07	8.10	3.80	58493	94	7.3×10^{-2}
47	24.89	1.56	11.01	2.70	57764	22	7.8×10^{-2}
23	238.14	18.42	8.52	3.03	57173	5	8.3×10^{-2}
90	217.59	0.03	9.40	2.55	57646	29	8.4×10^{-2}
104	165.83	−23.82	6.90	3.12	58904	20	8.6×10^{-2}
11	307.86	1.36	3.16	2.04	57056	7	9.5×10^{-2}
27	180.53	3.88	13.77	3.69	56470	26	9.6×10^{-2}
101	312.19	26.04	4.81	2.65	58692	5	0.10
100	127.71	12.14	7.16	2.61	57214	5	0.11
44	350.80	−14.90	5.34	3.08	57862	13	0.11
12	115.82	−10.53	4.32	2.61	58701	19	0.11
52	326.72	27.49	5.81	1.91	57677	5	0.11
115	194.94	1.74	5.59	2.61	58529	6	0.12
6	266.87	13.40	6.67	2.39	55551	37	0.12
36	33.62	9.90	4.87	1.98	55815	10	0.12
25	171.74	26.44	11.23	2.67	58063	120	0.12
73	188.33	−6.10	9.37	2.68	56698	78	0.12
16	68.36	40.82	3.93	1.66	58434	23	0.13
4	141.48	47.48	20.87	2.54	57931	268	0.13
50	48.32	0.49	17.16	3.53	55870	52	0.19
52	91.68	12.14	10.51	3.43	57694	12	0.20
2	298.56	11.55	8.18	2.67	56998	13	0.22
108	168.46	11.80	7.88	2.61	57075	7	0.23
103	226.14	10.77	5.93	2.55	55500	9	0.25
109	255.82	27.00	13.24	2.92	58940	32	0.25
28	70.81	19.08	8.34	2.85	58293	12	0.25
7	331.46	10.71	11.97	3.13	57753	18	0.26
105	4.80	−0.81	10.26	2.77	57854	21	0.28
74	77.50	2.55	12.44	2.49	57407	144	0.29
34	224.10	−4.09	5.26	4.00	56352	17	0.32
5	306.55	19.63	10.43	2.84	57728	37	0.33
121	271.00	25.11	18.65	4.00	56858	125	0.33

Continued on next page

Table 5 – continued from previous page

Index	R.A. [deg]	Dec [deg]	$\hat{n}_S$	$\hat{\gamma}$	$\hat{\mu}_T$	$\hat{\sigma}_T$	p_{local}
54	54.06	34.00	5.54	2.38	55465	8	0.34
78	227.37	30.25	7.27	4.00	56554	6	0.34
110	142.35	2.82	9.97	3.29	57011	10	0.34
113	265.01	5.34	11.57	2.66	58747	137	0.35
62	79.41	5.00	8.33	2.77	55881	23	0.36
51	100.95	4.98	13.56	2.74	57683	43	0.36
59	195.23	19.76	5.95	1.95	57777	43	0.37
72	26.38	9.71	2.64	1.83	55869	20	0.38
3	347.47	24.93	19.50	4.00	58817	67	0.39
40	193.20	−3.22	4.72	3.27	56069	5	0.39
61	261.34	−2.58	2.18	2.23	56311	5	0.40
47	110.83	11.64	3.10	2.01	56284	5	0.40
86	173.25	−2.54	5.89	3.94	58914	8	0.40
31	353.16	−1.40	4.50	2.61	57485	5	0.41
106	317.26	12.24	10.38	2.17	55648	194	0.42
69	200.71	−31.94	9.17	2.68	57641	149	0.46
81	207.80	26.04	6.19	2.04	57909	35	0.47
8	88.50	0.46	3.75	4.00	58729	5	0.47
35	130.17	−10.28	1.97	3.46	55727	5	0.48
37	301.37	10.50	4.16	2.06	56186	59	0.48
32	166.79	21.76	17.27	3.06	58039	105	0.48
26	329.40	1.12	10.31	4.00	57346	20	0.49
96	307.97	−32.03	5.75	2.71	58223	130	0.49
55	133.55	27.71	12.73	4.00	57202	96	0.49
65	151.05	14.93	10.71	2.69	56073	74	0.50
102	341.35	11.01	23.55	3.50	55932	225	0.50
53	327.92	5.82	7.41	3.54	57307	5	0.51
10	284.83	3.32	2.92	1.95	58860	51	0.52
1	29.51	1.23	4.52	4.00	58152	5	0.52
97	228.25	−4.44	4.67	4.00	57925	23	0.54
18	9.38	7.59	2.45	1.76	56920	133	0.55
114	105.55	6.38	10.56	3.26	57438	73	0.55
98	268.20	−16.29	8.79	3.93	55171	32	0.56
75	47.55	15.44	6.99	2.85	56015	6	0.56
19	199.21	8.87	9.84	3.33	58512	16	0.58
21	223.65	1.67	6.06	2.04	57754	58	0.59
46	105.67	0.97	8.75	2.52	56044	62	0.60
49	168.88	−1.43	12.14	4.00	57034	135	0.60
88	340.60	7.59	6.69	4.00	56225	10	0.63
122	60.12	−3.99	4.24	4.00	57539	33	0.64
20	266.67	−5.10	9.44	3.81	57444	122	0.65
79	282.81	8.26	16.67	2.98	57871	144	0.66
92	144.78	−2.95	12.23	4.00	58406	95	0.67
91	307.53	−4.97	6.03	2.39	57105	26	0.68
95	130.33	36.92	10.91	4.00	55469	51	0.68
82	359.34	4.36	11.18	3.54	56650	26	0.68
80	230.45	23.54	8.44	2.91	56927	13	0.68

Continued on next page

Table 5 – continued from previous page

Index	R.A. [deg]	Dec [deg]	$\hat{n}_S$	$\hat{\gamma}$	$\hat{\mu}_T$	$\hat{\sigma}_T$	p_{local}
112	29.00	3.47	3.64	4.00	57045	5	0.69
93	270.56	−7.29	6.61	2.10	58532	44	0.69
70	237.20	1.14	16.00	3.27	56123	65	0.70
22	37.14	18.69	16.67	2.89	57494	112	0.73
66	354.64	1.73	4.05	2.30	57815	5	0.73
119	207.07	13.27	6.99	3.26	56078	20	0.74
25	199.80	32.58	6.94	2.41	55763	38	0.74
39	289.35	−15.33	3.13	3.60	58116	8	0.75
63	263.76	−15.07	5.68	3.72	57964	136	0.76
15	272.55	36.20	5.39	1.97	55850	40	0.76
57	102.85	3.77	5.77	4.00	57412	5	0.77
77	97.34	−15.06	2.86	3.94	57966	5	0.79
111	96.46	−5.08	3.54	3.78	55790	14	0.80
117	6.66	−9.98	9.12	3.27	55227	69	0.82
94	25.91	7.61	24.88	3.40	56859	99	0.82
84	39.94	13.64	23.44	4.00	58516	221	0.83
14	235.34	19.76	10.65	2.42	58482	76	0.84
58	194.20	−3.81	6.96	2.76	55443	224	0.84
89	77.12	7.68	4.52	4.00	57329	5	0.84
76	310.55	6.39	9.45	2.80	55956	23	0.85
67	214.12	−0.71	6.49	3.58	57509	22	0.87
29	205.30	−2.65	6.59	3.19	56484	7	0.87
64	312.23	60.79	5.30	2.32	56903	7	0.88
13	137.87	−2.87	20.28	3.26	57963	386	0.90
9	111.16	−0.21	6.61	2.97	58059	19	0.90
68	122.43	−1.08	9.92	3.52	55389	127	0.91
56	280.64	30.35	12.20	2.57	57865	153	0.91
116	30.54	−11.15	3.03	2.49	57403	5	0.93
41	345.19	1.40	8.92	3.69	55980	35	0.93
42	293.51	33.32	4.21	4.00	56102	5	0.94
38	287.16	19.47	10.07	4.00	55637	45	0.96
45	346.71	18.24	12.32	2.61	55259	143	0.97
118	263.21	42.52	6.51	3.44	56064	6	0.98
71	191.42	35.21	4.87	1.60	55301	42	0.99

REFERENCES

Aartsen, M., Ackermann, M., Adams, J., et al. 2020, Journal of Instrumentation, 15, P06032, doi: 10.1088/1748-0221/15/06/P06032

Aartsen, M. G., Ackermann, M., Adams, J., et al. 2015, The Astrophysical Journal, 807, 46

—. 2017a, Journal of Instrumentation, 12, P03012, doi: 10.1088/1748-0221/12/03/P03012

—. 2017b, Astroparticle Physics, 92, 30, doi: 10.1016/j.astropartphys.2017.05.002

—. 2020, Physical Review Letters, 124, doi: 10.1103/physrevlett.124.051103

Aartsen, M. G., et al. 2018a, Science, 361, eaat1378, doi: 10.1126/science.aat1378

—. 2018b, Science, 361, 147, doi: 10.1126/science.aat2890

Abbasi, R., Abdou, Y., Abu-Zayyad, T., Adams, J., et al. 2011, The Astrophysical Journal, 732, 18, doi: 10.1088/0004-637x/732/1/18

Abbasi, R., Ackermann, M., Adams, J., et al. 2023a, IceCat-1: the IceCube Event Catalog of Alert Tracks. https://arxiv.org/abs/2304.01174

Abbasi, R., Ackermann, M., Adams, J., Aguilar, J. A., et al. 2021a, Phys. Rev. D, 104, 022002, doi: 10.1103/PhysRevD.104.022002

—. 2021b, arXiv e-prints, arXiv:2101.09836. https://arxiv.org/abs/2101.09836

—. 2021c, ApJL, 920, L45, doi: 10.3847/2041-8213/ac2c7b

—. 2022a, Science, 378, 538, doi: 10.1126/science.abg3395

—. 2022b, ApJ, 928, 50, doi: 10.3847/1538-4357/ac4d29

Abbasi, R., et al. 2021d, Astrophys. J., 911, 67, doi: 10.3847/1538-4357/abe7e6

Abbasi, R., Ackermann, M., Adams, J., et al. 2023b, The Astrophysical Journal, 951, 45, doi: 10.3847/1538-4357/acd2ca

Abdo, A. A., Ackermann, M., Ajello, M., et al. 2010, ApJS, 188, 405, doi: 10.1088/0067-0049/188/2/405

Acero, F., Ackermann, M., Ajello, M., et al. 2015, ApJS, 218, 23, doi: 10.1088/0067-0049/218/2/23

Ackermann, M., Ajello, M., Albert, A., et al. 2012, The Astrophysical Journal Supplement Series, 203, 4, doi: 10.1088/0067-0049/203/1/4

Bartoli, B., Bernardini, P., Bi, X. J., et al. 2013, The Astrophysical Journal, 779, 27. http://stacks.iop.org/0004-637X/779/i=1/a=27

Bianchi, L., Efremova, B., Herald, J., et al. 2011, MNRAS, 411, 2770, doi: 10.1111/j.1365-2966.2010.17890.x

Blaufuss, E., Kintscher, T., Lu, L., & Tung, C. F. 2019, in Proceedings of 36th International Cosmic Ray Conference — PoS(ICRC2019), Vol. 358, 1021, doi: 10.22323/1.358.1021

Boller, T., Freyberg, M. J., Trümper, J., et al. 2016, aap, 588, A103, doi: 10.1051/0004-6361/201525648

Braun, J., Baker, M., Dumm, J., et al. 2010, Astroparticle Physics, 33, 175, doi: 10.1016/j.astropartphys.2010.01.005

Braun, J., Dumm, J., De Palma, F., et al. 2008, Astropart. Phys., 29, 299, doi: 10.1016/j.astropartphys.2008.02.007

Condon, J. J., Cotton, W. D., Greisen, E. W., et al. 1998, AJ, 115, 1693, doi: 10.1086/300337

D'Elia, V., Perri, M., Puccetti, S., et al. 2013, A&A, 551, A142, doi: 10.1051/0004-6361/201220863

Dempster, A. P., Laird, N. M., & Rubin, D. B. 1977, Journal of the Royal Statistical Society. Series B (Methodological), 39, 1. http://www.jstor.org/stable/2984875

Eller, P., & Shtembari, L. 2021, A goodness-of-fit test based on a recursive product of spacings, arXiv, doi: 10.48550/ARXIV.2111.02252

Evans, P. A., Osborne, J. P., Beardmore, A. P., et al. 2014, The Astrophysical Journal Supplement Series, 210, 8. http://stacks.iop.org/0067-0049/210/i=1/a=8

Giommi, P., Arrigo, G., Barres De Almeida, U., et al. 2018, arXiv e-prints, arXiv:1805.08505. https://arxiv.org/abs/1805.08505

Gregory, P. C., Scott, W. K., Douglas, K., & Condon, J. J. 1996, ApJS, 103, 427, doi: 10.1086/192282

Haack, C., & Wiebusch, C. 2017, in Proceedings of 35th International Cosmic Ray Conference — PoS(ICRC2017), Vol. 301, 1005, doi: 10.22323/1.301.1005

Healey, S. E., Romani, R. W., Taylor, G. B., et al. 2007, ApJS, 171, 61, doi: 10.1086/513742

Jackson, N., Battye, R. A., Browne, I. W. A., et al. 2007, MNRAS, 376, 371, doi: 10.1111/j.1365-2966.2007.11442.x

Karl, M. 2019, in International Cosmic Ray Conference, Vol. 36, 36th International Cosmic Ray Conference (ICRC2019), 929. https://arxiv.org/abs/1908.05162

Karl, M., & Eller, P. 2023, Fitting neutrino flares: Applying expectation maximization on neutrino data. https://arxiv.org/abs/2312.15196

Karl, M., Eller, P., & Schubert, A. 2021, in Proceedings of 37th International Cosmic Ray Conference — PoS(ICRC2021), Vol. 395, 940, doi: 10.22323/1.395.0940

Karl, M., Abbasi, R., Ackermann, M., et al. 2023, in Proceedings of 38th International Cosmic Ray Conference — PoS(ICRC2023), Vol. 444, 974, doi: 10.22323/1.444.0974

Karl, M. S. 2022, Dissertation, Technische Universität München, München

Kintscher, T. 2016, Journal of Physics: Conference Series, 718, 062029, doi: 10.1088/1742-6596/718/6/062029

Kronmueller, M., & Glauch, T. 2019, Application of Deep Neural Networks to Event Type Classification in IceCube. https://arxiv.org/abs/1908.08763

Myers, S. T., Jackson, N. J., Browne, I. W. A., et al. 2003, MNRAS, 341, 1, doi: 10.1046/j.1365-8711.2003.06256.x

Nieppola, E., Tornikoski, M., Lähteenmäki, A., et al. 2007, AJ, 133, 1947, doi: 10.1086/512609

Nolan, P. L., Abdo, A. A., Ackermann, M., et al. 2012, ApJS, 199, 31, doi: 10.1088/0067-0049/199/2/31

Padovani, P., Giommi, P., Falomo, R., et al. 2022, MNRAS, 510, 2671, doi: 10.1093/mnras/stab3630

Planck Collaboration, Ade, P. A. R., Aghanim, N., et al. 2011, A&A, 536, A7, doi: 10.1051/0004-6361/201116474

—. 2014, A&A, 571, A28, doi: 10.1051/0004-6361/201321524

—. 2015, ArXiv e-prints. https://arxiv.org/abs/1507.02058

Voges, W., Aschenbach, B., Boller, T., et al. 1999, A&A, 349, 389

Waxman, E., & Bahcall, J. N. 1999, Phys. Rev., D59, 023002, doi: 10.1103/PhysRevD.59.023002

White, R. L., & Becker, R. H. 1992, ApJS, 79, 331, doi: 10.1086/191656

Wilks, S. S. 1938, The Annals of Mathematical Statistics, 9, 60 , doi: 10.1214/aoms/1177732360

Wright, A. E., Griffith, M. R., Burke, B. F., & Ekers, R. D. 1994, ApJS, 91, 111, doi: 10.1086/191939

Wright, E. L., Eisenhardt, P. R. M., Mainzer, A. K., et al. 2010, AJ, 140, 1868, doi: 10.1088/0004-6256/140/6/1868